Title: Surface Waves and Crustal Structure on Mars

Authors: D. Kim[1]*, W. B. Banerdt[2], S. Ceylan[1], D. Giardini[1], V. Lekic[3], P. Lognonné[4], C. Beghein[5], É. Beucler[6], S. Carrasco[7], C. Charalambous[8], J. Clinton[9], M. Drilleau[10], C. Durán[1], M. Golombek[2], R. Joshi[11], A. Khan[1,12], B. Knapmeyer-Endrun[7], J. Li[5], R. Maguire[13], W. T. Pike[7], H. Samuel[4], M. Schimmel[14], N. Schmerr[3], S. C. Stähler[1], E. Stutzmann[4], M. Wieczorek[15], Z. Xu[4], A. Batov[16], E. Bozdag[17], N. Dahmen[1], P. Davis[5], T. Gudkova[16], A. Horleston[18], Q. Huang[17], T. Kawamura[4], S. King[19], S. M. McLennan[20], F. Nimmo[21], M. Plasman[4], A. C. Plesa[22], I. E. Stepanova[16], E. Weidner[5], G. Zenhäusern[1], I. J. Daubar[23], B. Fernando[24], R. Garcia[9], L. V. Posiolova[25], M. P. Panning[2]

Affiliations:

[1]Institute of Geophysics, ETH Zürich, Zürich, Switzerland
[2]Jet Propulsion Laboratory, California Institute of Technology, Pasadena, CA, USA
[3]Department of Geology, University of Maryland, College Park, MD, USA
[4]Université de Paris, Institut de Physique du Globe de Paris, CNRS, Paris, France
[5]Department of Earth, Planetary and Space Sciences, University of California, Los Angeles, CA, USA
[6]Laboratoire de Planétologie et Géodynamique, UMR6112, Université de Nantes, Université dAngers, CNRS, Nantes, France
[7]Bensberg Observatory, University of Cologne, Bergisch Gladbach, Germany
[8]Department of Electrical and Electronic Engineering, Imperial College London, London, UK
[9]Swiss Seismological Service, ETH Zürich, Zürich, Switzerland
[10]Institut Supérieur de l'Aéronautique et de l'Espace SUPAERO, Toulouse, France
[11]Max Planck Institute for Solar System Research, Göttingen, Germany
[12]Physik-Institut, University of Zürich, Zürich, Switzerland
[13]Department of Computational Mathematics, Science, and Engineering, Michigan State University, East Lansing, MI, USA
[14]Geosciences Barcelona – CSIC, Barcelona, Spain
[15]Université Côte d'Azur, Observatoire de la Côte d'Azur, CNRS, Laboratoire Lagrange, Nice, France
[16]Schmidt Institute of Physics of the Earth, Russian Academy of Sciences, Moscow, Russia
[17]Department of Geophysics, Colorado School of Mines, Golden, CO, USA
[18]School of Earth Sciences, University of Bristol, Bristol, UK
[19]Department of Geosciences, Virginia Tech, Blacksburg, VA, USA
[20]Department of Geosciences, Stony Brook University, Stony Brook, NY, USA
[21]Department of Earth and Planetary Sciences, University of California Santa Cruz, Santa Cruz, CA, USA
[22]Institute of Planetary Research, German Aerospace Center (DLR), Berlin, Germany
[23]Department of Earth, Environmental, and Planetary Sciences, Brown University, Providence, RI, USA
[24]Department of Earth Sciences, University of Oxford, Oxford, UK
[25]Malin Space Science Systems, San Diego, CA, USA

*Corresponding author. Doyeon Kim (doyeon.kim@erdw.ethz.ch)

Abstract:

We detected surface waves from two meteoroid impacts on Mars. By measuring group velocity dispersion along the impact-lander path, we obtained a direct constraint on crustal structure away from the *InSight* lander. The crust north of the equatorial dichotomy has a shear wave velocity of ~3.2 km/s in the 5-30 km depth range, with little depth-variation. This implies a higher crustal density than inferred beneath the lander, suggesting either compositional differences or reduced porosity in the volcanic areas traversed by the surface waves. The lower velocities and the crustal layering observed in the landing site down to 10 km depth are not a global feature. Structural variations revealed by surface waves hold implications for models of the formation and thickness of the martian crust.

One-Sentence Summary:

Surface waves detected by *InSight* from two large meteoroid impacts reveal lateral variations in crustal structure of Mars.

Main Text:

The martian crust exhibits striking variations in topography, inferred thickness, age, cratering, resurfacing and volcanism (*1*). Constraining the variation of crustal properties and composition with depth is crucial for understanding its origin and evolution (*2*). Inferences of crustal thickness and density variations, which are derived from joint analysis of topography and gravity data, suffer from substantial trade-offs (*3*). For example, the ~5 km topographic difference between the highly-cratered southern highlands and the low-lying, less cratered northern plains can be explained by differences in crustal thickness or by large variations in crustal density (*4*) or a combination thereof.

The *InSight* mission to Mars (*5*) has provided direct constraints on the layering of Mars' crust at the landing site (*6*). Analyses of body wave conversions and ambient noise wavefield have constrained the crustal thickness beneath the *InSight* lander in Elysium Planitia to be 39±8 km (*7-9*), providing a key anchoring-point for global models of crustal thickness and density variations. Looking deeper, travel times of body waves from several marsquakes have enabled the determination of seismic velocity profiles of the upper mantle (*10*) and core radius (*8, 11)* and mean density (*12*). Despite these achievements, competing effects of epicentral distance, source depth, and radial structure on body wave travel times (*13*), have stymied efforts to constrain lateral variations in structure using a single seismometer on Mars.

The velocity of surface waves, unlike that of body waves, depends on frequency, with lower-frequency waves sensitive to greater depths. The measurement of surface wave dispersion therefore provides a direct observation of the depth-dependent variation of seismic velocities averaged along the path from source to receiver (*14*). Until now surface waves had not been observed on any marsquake records. Their absence could be due to the relatively small magnitude of the recorded seismic events (*15*), large source depths (*8*) and/or contamination of seismic data by long-period wind noise as well as atmospheric pressure waves (*16*). Strong crustal scattering on Mars (*6, 17*) can also impede the propagation and affect the visibility of surface waves, as was the case on the Moon (*18)*.

We report here the first detection of surface waves on Mars, in the seismic waveforms of events S1094b and S1000a. S1094b, which occurred on December 24th, 2021, is the third-largest seismic event (M_W = 4.0±0.2) and has the longest-duration seismic signal recorded to date by InSight (*19*), with coda energy persisting for more than 135 minutes. Based on the differential

travel time of the direct P and S arrivals, and measured P-wave polarization, the initial distance and back azimuth estimates provided by the Marsquake Service were 59.7±6° and 40° (-9°, +18°), corresponding to a source region in Amazonis Planitia, ~3460 km northeast from InSight (Fig. 1). The Mars Reconnaissance Orbiter (MRO) images taken between December 24-25, 2021 reveal a large impact crater in Amazonis Planitia, 3532 km away from the lander and consistent with the source location estimated for S1094b (*20*). With similar broad frequency content and moment magnitude of S1094b, event S1000a has also been identified as atypical based on its seismic characteristics (*19*) and was recently associated with an impact crater near the Tharsis province, ~7460 km away from the InSight lander (*20*). The ground-truth identification of the two events as impacts removes all uncertainties related to hypocentral depth.

We apply standard marsquake data processing methodologies (*19*) to the S1094b waveform data. An unusually large amplitude seismic arrival is observed 800 s after the P-wave in the S-wave coda in the vertical-component spectrogram (Fig. 2). The arrival's frequency content is considerably lower than typical of P- and S-wave arrivals in low-frequency (LF) family marsquakes (*8, 10*). Narrow-band filter banks of the raw vertical-component data show dispersion in the 6-18 s period range (Fig. 2). Frequency-dependent polarization analysis confirms that particle motion is strongly elliptically-polarized in the vertical plane (fig. S1E). The systematic phase shift between the vertical and horizontal components suggests that the arrival has a predominantly retrograde particle motion and arrives from 51° due northeast, consistent with the polarization of the direct P-wave (fig. S6).

Taken together, these characteristics allow the positive identification of this phase as the minor-arc Rayleigh wave (R1). Although strong elliptical polarization has been previously observed in the 3-30 s period range of the ambient seismic noise recordings, they were strictly polarized in the horizontal plane (*17*) and correlated with daytime wind direction on Mars. Despite heavy late afternoon winds, a comodulation analysis of the potential wind injection during the R1 arrival documents excess seismic energy over that generated by wind between 8-15 s at the time of the observation (fig. S3). Moreover, we confirm that the seismic data recorded during the surface wave arrival is not contaminated by any known electro-mechanical artifacts associated with the seismic sensor or the InSight spacecraft system (*24*).

We find no evidence for Love waves in the S1094b records. This observation is consistent with an impact origin for S1094b, as an isotropic source would primarily excite Rayleigh waves. The detection of Rayleigh waves from this impact source, but not from other LF marsquakes, supports the argument that marsquakes recorded to date are generally too deep to effectively excite surface waves (*25*). Our waveform simulation confirms that surface waves from shallow seismic sources are far more likely to be detectable, given the diurnal ambient noise level on Mars (fig. S15).

We observed an additional anomalous seismic arrival approximately 75 minutes after the identified R1 (fig. S2). Like for the R1 observation, the time of this arrival is far outside the time window for a potential direct or ground-coupled infrasound wave originating from the impact source region (*20, 26*). However, the timing is consistent with that expected for the major-arc Rayleigh wave (R2), that propagated in the opposite direction around Mars. Dispersion and enhanced elliptical polarization in the vertical plane in the 6-11 s period range supports the R2 interpretation. While the frequency content of this arrival is comparable to that of R1, broadband environmental injection in the analysis window is also evident (fig. S4). Due to low signal-to-noise ratio, the direction of propagation and particle motion of this phase are unclear and thus the

identification of R2 is not definitive. We find no evidence for the arrival of surface wave overtones, nor multi-orbiting Rayleigh waves in the S1094b waveforms (*19*).

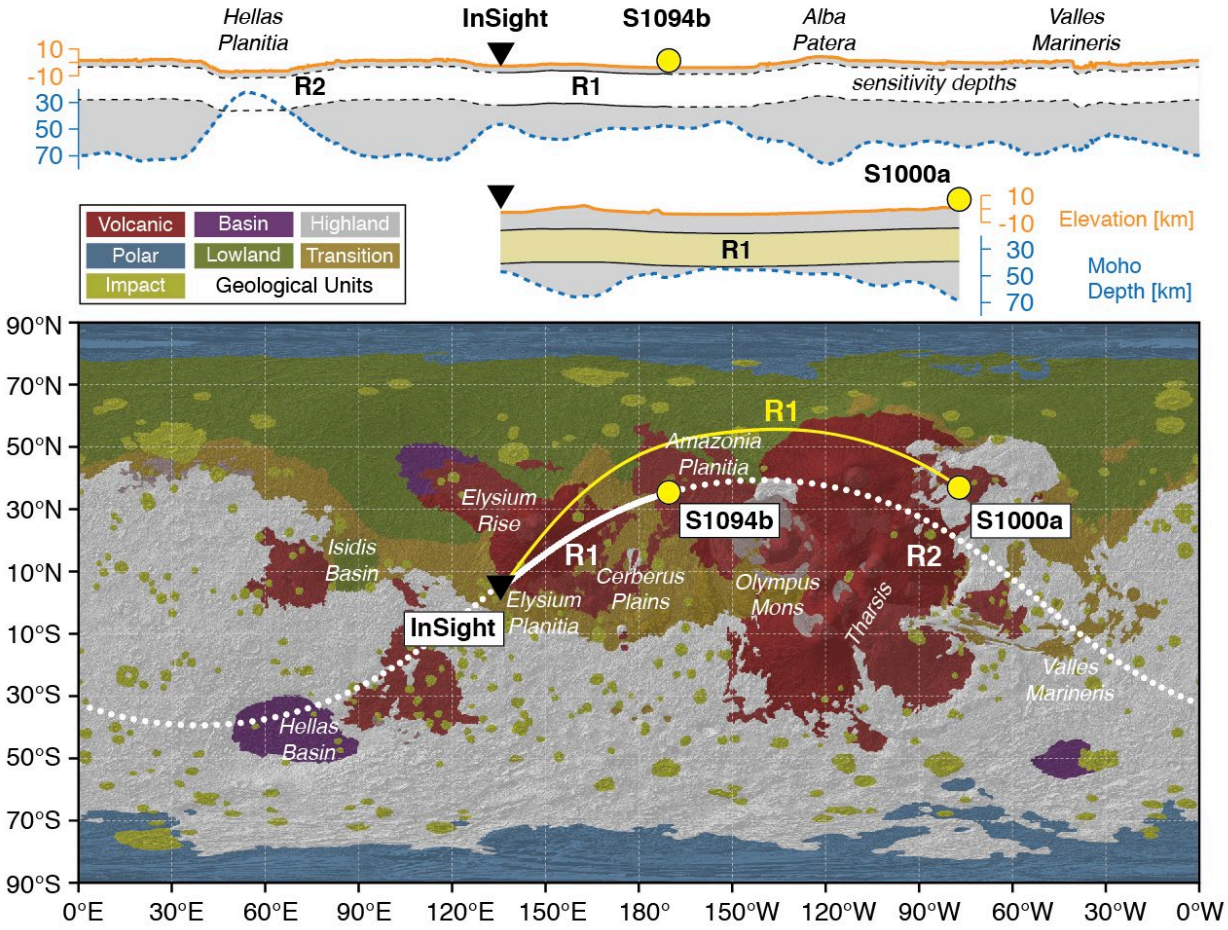

Figure 1. Locations of two large meteoroid impacts (yellow circles) identified in MRO images (*20*). The great circle paths for R1 (solid) and R2 (dashed) in S1094b are in white, while the R1 path for S1000a is in yellow. Background topographic relief is from the Mars Orbiter Laser Altimeter (*21*). The distribution and sequence of major geological unit groups of Hesperian and Amazonian age (*22*) are overlaid. Global elevation (orange) and the crust-mantle boundary depth profiles (*23*) along the R1 and R2 paths (dashed blue) are shown at the top.

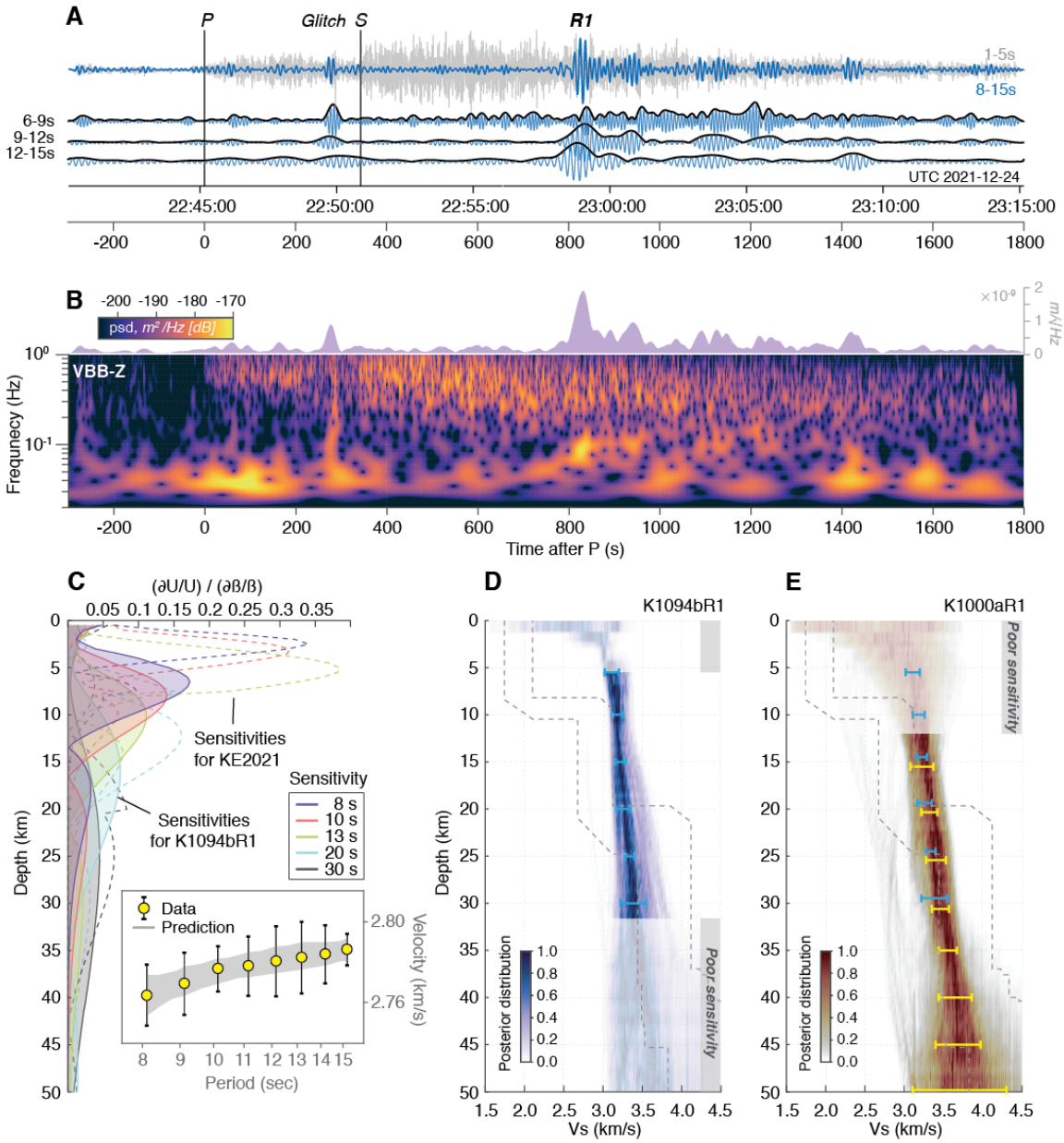

Figure 2. Seismic waveforms and velocity profiles. (**A**) Vertical-component seismogram of S1094b bandpass filtered between 1-5 s (gray) and 8-15 s (blue) with P and S wave picks (black vertical lines). Narrow-band filter banks and envelopes show dispersed signals 800 s after the P-wave. (**B**) The vertical component S-transform shows a large amplitude seismic arrival that exhibits dispersion (c.f., 2A). The frequency domain envelope averaged across the 8-15 s period range is plotted at the top of the spectrogram. Other characteristics enabling the identification of this dispersive arrival as R1 are shown in the Supplementary Materials (*19*). (**C**) Depth sensitivity kernels and data misfit of R1 in S01094b (inset). The mean and standard deviation are drawn from 10 pairs of dispersion measurements (fig. S7). Kernels in dashed lines are computed based on the three-layer crustal model in (*7*) denoted as KE2021. Note the substantial differences between the kernels due to different velocity profiles. Shaded kernels and predictions are computed using the average model in panel 2D. (**D**) Posterior distribution of V_S structure inverted from the group velocity measurements of S1094b R1 (K1094bR1). Posterior distribution and prediction are based on the best-fitting 10,000 models after one million iterations. Depths where sensitivity is inadequate (<40% in cumulative kernel strength) are muted. The range of V_S in the three-layer crustal models beneath the lander (*7*) are indicated by gray dashed lines. (**E**) Posterior distribution of the V_S structure inverted with the group velocity measurements of the potential S1000a R1 (K1000aR1) at ~20 s and ~30 s period (fig. S13).

Surface wave data on Earth are typically interpreted assuming that propagation occurs along the great circle path from source to receiver, and that it can be related to the average flat-layer structure along that path (*27*). Using a number of crustal thickness models constructed based on gravimetric data and the extrapolated crustal thickness estimates from the InSight location (*23*), our kinematic ray tracing predicts negligible deviations from great circle paths for R1 and R2, less than 0.2% of the total travel time (*19*). We measured the group velocities of R1 and R2 and obtained average values of 2.77 and 3.14 km/s, respectively, which imply structural differences along their propagation paths (fig. S7). Indeed, while the R1 path traverses only the northern lowlands, a large fraction of the R2 path crosses the southern highlands and between 12% and 17% of the path passes through the Hellas impact basin, where the crust has been largely removed and replaced by uplifted mantle (*28*). Consequently, the crustal thickness within the Hellas impact basin could be as low as a few kilometers (*23*) and R2 would travel at seismic velocities characteristic of the uppermost mantle (V_S 4-4.5 km/s) at periods of 10-16 s. The observed higher value in the average group velocity of R2 with respect to R1 could then be accounted for by Hellas alone and as a result the average crustal velocity of the southern and northern hemispheres would be very similar (fig. S19).

Notably, both phases show little dispersion in the observed frequency range, which is primarily sensitive to crustal structure between ~5-30 km depth (Fig. 2C). We inverted for path-averaged radial P- and S-wave velocity profiles using the R1 measurements with multiple approaches (Fig. 2C, and figs. S9-S11) and regardless of the parameterization strategies considered (*19*), we obtained a uniform V_S of about 3.2 km/s, with a slight linear increase down to 30 km depth. At greater depths, we lose sensitivity due to lack of dispersion measurements at long periods (Fig. 2). At shallowest depths, we cannot rule out a thin slow layer, though due to the non-linear relationship between V_S profiles and surface wave sensitivity kernels (Fig. 2C), the greatest permissible thickness of such a layer depends on its V_S. The uniform V_S in the 5-30 km crustal depth range is different from the three-layer crustal structure observed beneath InSight (*7-9*). The obtained V_S is substantially higher in the upper 10 km and is similar to the average velocities of the second and third layers beneath the lander (Fig. 2D), but does not show the same velocity jump around 20 km depth. From the comparison of the local and the R1 path-average velocity structures, we conclude that the low V_S observed down to 8-10 km depth below the lander is a local feature and if present in other parts along the path it must be restricted to only few kilometers below the surface. We cannot exclude the presence of deeper layering in the crust, but this would have to occur at varying depths along the path, to be averaged in the observed linear V_S increase with depth.

The high crustal seismic velocities inferred from the S1094b dispersion analysis are supported by S1000a data. Two distinct long-period arrivals, at ~20 s and ~30 s periods, are visible in the vertical-component spectrogram of S1000a in the R1 group arrival time range predicted based on the posterior distribution of V_S (fig. S12). While R1 in S1094b shows clear polarization, the comparative strength of the environmental injection during the expected R1 window of S1000a prevents a definitive identification. The inferred V_S structure using the S1000a group velocity measurements at ~20 s and ~30 s periods (2.73 km/s and 2.83 km/s) overlaps with our posterior V_S distribution based on group velocities of R1 for S1094b down to 30 km depth and provides additional constraints to image a slowly increasing V_S in the lower crust down to 45 km depth (Fig. 2E). This agreement suggests a high degree of similarity in the average crustal structure along the two R1 paths

Unlike dispersion, the frequency-dependence of Rayleigh wave ellipticity, expressed as the ratio of horizontal-to-vertical amplitude (H/V), is strongly sensitive to the structure directly beneath InSight. We find that the H/V measurements made on R1 are consistent with previous models of crustal layering directly beneath InSight (figs. S16, S17), as are P-to-s conversions in the P-wave

coda of S1094b which show prominent arrivals at 2.4 s, 4.8 s, and 7.2 s after the direct P arrival (figs. S20, S21). Even with a single event, we can confirm that the shallow crustal structure at the landing site down to 10 km depth is substantially slower than the average crustal velocity sampled by the R1 path.

The observed surface waves allow us to expand the current understanding of crustal structure on Mars beyond the crustal layering inferred beneath the InSight landing site (*7*). We find that the low V_S layer extending down to 10 km depth in the shallow crust of Elysium Planitia does not exist globally on Mars. Instead, the average crustal velocities along the R1 paths of S1000a and S1094b (Fig. 3) are considerably faster and are likely to be more representative of average crustal structure. Large geographic variations in upper crustal structure hold implications for interpreting waveforms of surface-bouncing seismic waves such as PP and SS, and must be explicitly accounted for when constructing models of the spherically-symmetric structure of Mars. Relatedly, these structural variations hold clues for the deeper signature of surface geologic units and for interpretations of gravity data.

A large portion of the R1 paths between Elysium and Amazonis Planitiae passes through the Elysium rise, the largest volcanic province in the northern lowlands (Fig. 1). Its surface geology is characterized by lava flows of Hesperian to Amazonian age, reaching up to several kilometers of thickness and representing a history of major resurfacing (*29*). Beyond Elysium, the S1000a R1 path again encounters extensive regions covered by Hesperian and Amazonian volcanics in Amazonis Planitia and north of Alba Patera. In contrast, the plains around the InSight lander are composed of Early Hesperian and Early Amazonian lava flows (*30, 31*) whose limited thickness is insufficient to affect R1 dispersion. Below ~200 m, weaker sedimentary material is suggested to extend in places at least to 5-6 km depth based on the phyllosilicate signatures and layered sedimentary rocks brought up in the central peaks of large impact craters (*32*).

Similar constraints are provided by density inferred from gravity data. The maximum permissible density of the overall crust on Mars (2850-3100 kg/m^3) is lower than the density of most martian basaltic materials found at the surface, as estimated by gamma-ray compositional mapping (*33*) and by mineralogical norms for SNC meteorites of predominantly Amazonian age (see summary in *23*). The two factors contributing to a layered crustal density structure on a global scale could be a less mafic (less dense) composition and/or an elevated porosity (*6, 7, 23*) (Fig. 3).

As most of the R1 paths pass through regions resurfaced by relatively young volcanic rocks, this would result in similar, higher densities of the upper and lower crust. Although Elysium volcanic cumulates are only a few kilometers thick (*22*) and thus within the uppermost zone of poor seismic sensitivity (Fig. 2), their magmatic history influenced the nature of the whole crust in this region (*34, 35*). The average ratio of intrusive/extrusive magmatism on Mars (*36*, *37*) implies that intrusives account for >5 km of average crustal thickness integrated over the entire Elysium rise, and even more near the volcanic centers traversed by R1 (Fig. 1). One proposal for Mars is that intrusive rocks (i.e. magma chamber centers) would concentrate at greater depths than on Earth (*34*). These intrusive magmas represent, at least in part, residues of the partial melting giving rise to surface lavas and so likely are of greater density (*38*) and elevated seismic wave speeds closer to values typical of basaltic volcanic rocks, consistent with the path-average velocity profiles we observe below 5 km depth (Fig. 2).

Substantial porosity is also likely to be present in the upper crustal layers beneath the lander (*6, 7, 23*). Their low V_S is compatible with fractured basalt having, for example, 10% porosity, though the exact amount depends strongly on both the aspect ratio of the pore spaces and material contained therein (fig. S22). However, the higher path-averaged velocities we observe in the upper 10 km would require lower porosity, which could result from viscous closure of pore spaces due

to thermal annealing expected to accompany volcanic resurfacing processes (*23, 39*), partial filling of pore spaces by the deposition of precipitated minerals from a briny ancient aquifer system (*40*), or the presence of a deep cryosphere or substantial water table beneath the thick Amazonian lava flows along the R1 path (*19, 41, 42*) (Fig. 3). We note that images from the High Resolution Imaging Science Experiment of the S1094b impact crater show large blocks of pure ice ejected from the shallower layers (*20*). This would not be expected to be the case near InSight, because the shallow crust with V_S of 1.7-2.1 km/s in the upper 8-11 km (*7*) rules out an ice-saturated cryosphere (*40*).

Another possibility is that a low density, high porosity layer beneath InSight results from ejecta deposited by the Utopia impact *(23)*. Because ejecta thickness is a strong function of radial distance, one would expect the ejecta thickness averaged along the R1 path to be much less than beneath InSight, consistent with the observations.

Regardless of the exact origin – composition and/or porosity – variations of crustal seismic structure presented here are likely correlated with density variations, because both temperature and compositional variations increase density together with V_S, and our results imply greater crustal densities between Elysium and Amazonis Planitiae than directly beneath the lander. This result is consistent with previous estimates of higher crustal density beneath the Elysium rise of 3100±100 kgm^{-3} (*43*) and lower density beneath the lander (*44*) from gravity-topography measurements. Density variations would also affect inferences of crustal thickness from topographic and gravity signals associated with the crustal dichotomy (*4, 23*). Currently, both exogenic (i.e., one or more large impacts; *45*) and endogenic (i.e., mantle convection) processes (*46*), or a combination thereof (*47*) continue to be debated as the origin of the dichotomy. Both processes would be expected to generate a basaltic secondary crust in the northern lowlands, consistent with the R1 observations from the two recent impacts. However, if confirmed by further analyses or other events, the S1094b R2 observation of similar group velocities across the southern hemisphere (once corrected for the path in the Hellas impact basin) preliminarily indicates that the crustal structure at relevant depths could be substantially similar North and South of the dichotomy (Fig. 3).

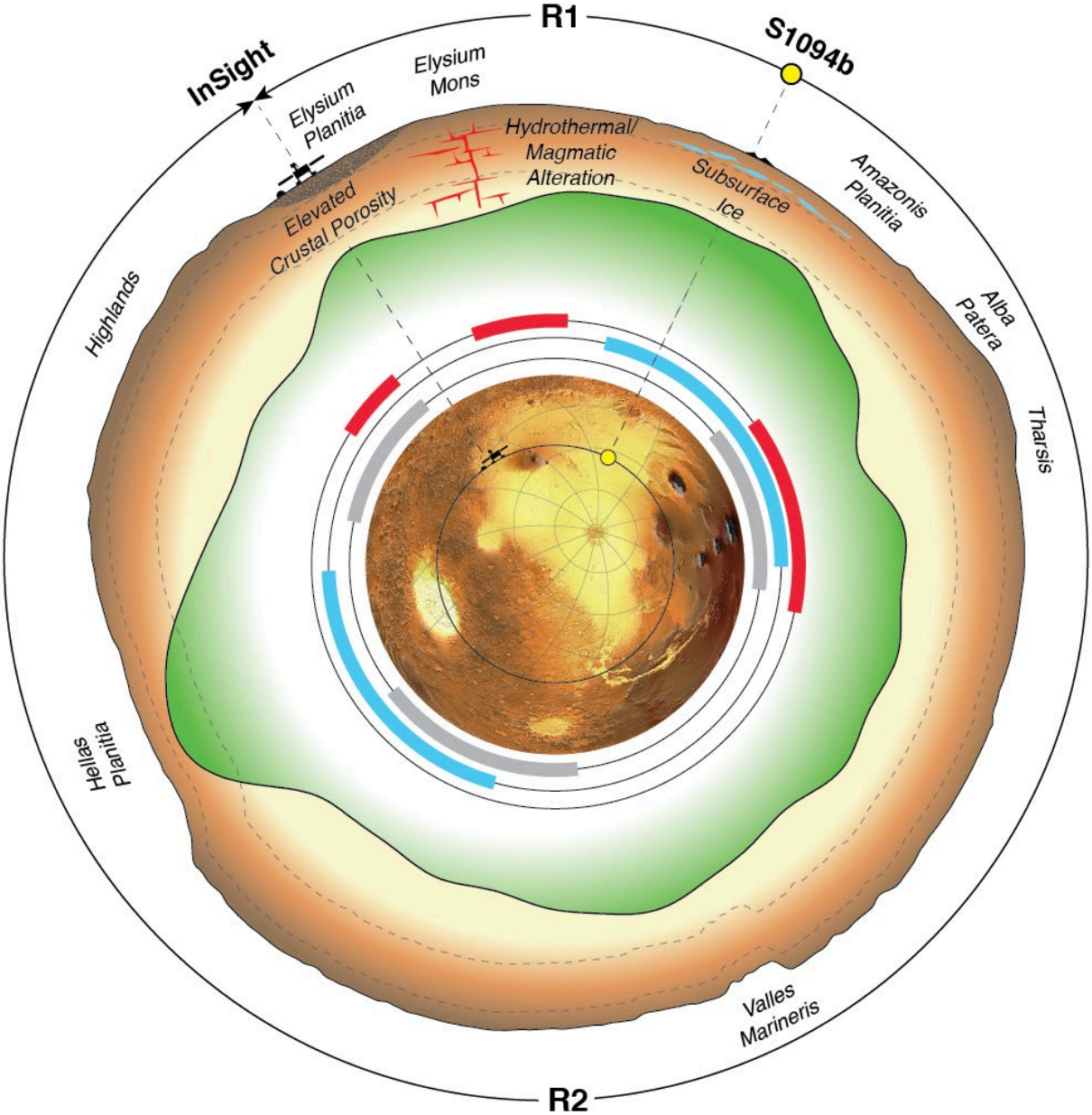

Figure 3. Cross section of the S1094b surface wave path through Mars. Surface topography (*21*) and crustal thickness (*23*) with a 20x vertical exaggeration are shown along the path of R1 and R2, with major geological provinces labeled at the surface and potential subsurface structures that affect surface wave velocity. The approximate sampling depth of the observed surface waves is indicated by gray dashed line. The inset context map shows the topography along the surface wave paths. The colored arcs indicate the path length(s) through provinces with surface volcanism (red), ice stability at latitudes > 30º (cyan), and cratered highlands (gray).

References and Notes

1. Taylor, S. R., & McLennan, S. M. (2009). Planetary crusts: Their composition, origin, nd evolution. Cambridge: Cambridge Univ. Press.
2. Smrekar, S.E., Lognonné, P., Spohn, T., Banerdt, W.B., Breuer, D., Christensen, U., Dehant, V., Drilleau, M., Folkner, W., Fuji, N. and Garcia, R.F., 2019. Pre-mission InSights on the interior of Mars. Space Science Reviews, 215(1), pp.1-72.
3. Zuber, M.T., 2001. The crust and mantle of Mars. Nature, 412(6843), pp.220-227.

4. Belleguic, V., Lognonné, P., Wieczorek, M., *Journal of Geophysical Research: Planets*, **110**(E11) (2005).
5. Banerdt, W. B., Smrekar, S. E., Banfield, D., Giardini, D., Golombek, M., Johnson, C. L., ... & Wieczorek, M. (2020). Initial results from the InSight mission on Mars. Nature Geoscience, 13(3), 183-189.
6. Lognonné, P., Banerdt, W.B., Pike, W.T., Giardini, D., Christensen, U., Garcia, R.F., Kawamura, T., Kedar, S., Knapmeyer-Endrun, B., Margerin, L. and Nimmo, F., 2020. Constraints on the shallow elastic and anelastic structure of Mars from InSight seismic data. Nature Geoscience, 13(3), pp.213-220.
7. Knapmeyer-Endrun, B., Panning, M.P., Bissig, F., Joshi, R., Khan, A., Kim, D., Lekić, V., Tauzin, B., Tharimena, S., Plasman, M. and Compaire, N., 2021. Thickness and structure of the martian crust from InSight seismic data. Science, 373(6553), pp.438-443.
8. Durán, C., Khan, A., Ceylan, S., Zenhäusern, G., Stähler, S., Clinton, J.F. and Giardini, D., 2022. Seismology on Mars: An analysis of direct, reflected, and converted seismic body waves with implications for interior structure. Physics of the Earth and Planetary Interiors, p.106851.
9. Kim, D., Lekić, V., Irving, J.C., Schmerr, N., Knapmeyer-Endrun, B., Joshi, R., Panning, M.P., Tauzin, B., Karakostas, F., Maguire, R. and Huang, Q., 2021. Improving constraints on planetary interiors with PPs receiver functions. Journal of Geophysical Research: Planets, 126(11), p.e2021JE006983.
10. Khan, A., Ceylan, S., van Driel, M., Giardini, D., Lognonné, P., Samuel, H., Schmerr, N.C., Stähler, S.C., Duran, A.C., Huang, Q. and Kim, D., 2021. Upper mantle structure of Mars from InSight seismic data. Science, 373(6553), pp.434-438.
11. Stähler, S.C., Khan, A., Banerdt, W.B., Lognonné, P., Giardini, D., Ceylan, S., Drilleau, M., Duran, A.C., Garcia, R.F., Huang, Q. and Kim, D., 2021. Seismic detection of the martian core. Science, 373(6553), pp.443-448.
12. Khan, A., Sossi, P. A., Liebske, C., Rivoldini, A., & Giardini, D. (2022). Geophysical and cosmochemical evidence for a volatile-rich Mars. *Earth and Planetary Science Letters*, 578, 117330.
13. Khan, A., van Driel, M., Böse, M., Giardini, D., Ceylan, S., Yan, J., ... & Banerdt, W. B. (2016). Single-station and single-event marsquake location and inversion for structure using synthetic Martian waveforms. Physics of the Earth and Planetary Interiors, 258, 28-42.
14. Toksöz, M.N. and Anderson, D.L., 1966. Phase velocities of long-period surface waves and structure of the upper mantle: 1. Great-Circle Love and Rayleigh wave data. Journal of Geophysical Research, 71(6), pp.1649-1658.
15. Böse, M., Stähler, S.C., Deichmann, N., Giardini, D., Clinton, J., Lognonné, P., Ceylan, S., van Driel, M., Charalambous, C., Dahmen, N. and Horleston, A., 2021. Magnitude scales for Marsquakes calibrated from InSight data. Bulletin of the Seismological Society of America, 111(6), pp.3003-3015.
16. Stutzmann, É., Schimmel, M., Lognonné, P., Horleston, A., Ceylan, S., van Driel, M., Stähler, S., Banerdt, B., Calvet, M., Charalambous, C. and Clinton, J., 2021. The polarization of ambient noise on Mars. Journal of Geophysical Research: Planets, 126(1), p.e2020JE006545.
17. van Driel, M., Ceylan, S., Clinton, J.F., Giardini, D., Horleston, A., Margerin, L., Stähler, S.C., Böse, M., Charalambous, C., Kawamura, T. and Khan, A., 2021. High-frequency seismic events on Mars observed by InSight. Journal of Geophysical Research: Planets, 126(2), p.e2020JE006670.
18. Dainty, A.M., Toksöz, M.N., Anderson, K.R., Pines, P.J., Nakamura, Y. and Latham, G., 1974. Seismic scattering and shallow structure of the Moon in Oceanus Procellarum. The Moon, 9(1), pp.11-29.

19. Materials and Methods are available as supplementary materials.
20. Posiolova et al., *Science*, in revision.
21. Smith, D.E., Zuber, M.T., Solomon, S.C., Phillips, R.J., Head, J.W., Garvin, J.B., Banerdt, W.B., Muhleman, D.O., Pettengill, G.H., Neumann, G.A. and Lemoine, F.G., 1999. The global topography of Mars and implications for surface evolution. science, 284(5419), pp.1495-1503.
22. Tanaka, K.L., Robbins, S.J., Fortezzo, C.M., Skinner Jr, J.A. and Hare, T.M., 2014. The digital global geologic map of Mars: Chronostratigraphic ages, topographic and crater morphologic characteristics, and updated resurfacing history. Planetary and Space Science, 95, pp.11-24.
23. Wieczorek, M. A., Broquet, A., McLennan, S. M., Rivoldini, A., Golombek M., Antonangeli, D., Beghein, C., Giardini, D., Gudkova, T., … 2022. InSight constraints on the global character of the Martian crust, Journal of Geophysical Research: Planets, e2022JE007298.
24. Kim, D., Davis, P., Lekić, V., Maguire, R., Compaire, N., Schimmel, M., Stutzmann, E., CE Irving, J., Lognonné, P., Scholz, J.R. and Clinton, J., 2021. Potential pitfalls in the analysis and structural interpretation of seismic data from the Mars InSight mission. Bulletin of the Seismological Society of America, 111(6), pp.2982-3002.
25. Giardini, D., Lognonné, P., Banerdt, W.B., Pike, W.T., Christensen, U., Ceylan, S., Clinton, J.F., van Driel, M., Stähler, S.C., Böse, M. and Garcia, R.F., 2020. The seismicity of Mars. Nature Geoscience, 13(3), pp.205-212.
26. Garcia, R. F., Murdoch, N., Lorenz, R., Spiga, A., Bowman, D. C., Lognonné, P., ... & Banerdt, W. B. (2021). Search for infrasound signals in InSight data using coupled pressure/ground deformation methods. Bulletin of the Seismological Society of America, 111(6), 3055-3064.
27. Moulik, P., Lekic, V., Romanowicz, B., Ma, Z., Schaeffer, A., Ho, T., Beucler, E., Debayle, E., Deuss, A., Durand, S. and Ekström, G., 2022. Global reference seismological data sets: multimode surface wave dispersion. Geophysical Journal International, 228(3), pp.1808-1849.
28. Wieczorek, M. A., & Phillips, R. J. (1999). Lunar multiring basins and the cratering process. Icarus, 139(2), 246-259.
29. Platz, T., & Michael, G. (2011). Eruption history of the Elysium volcanic province, Mars. Earth and Planetary Science Letters, 312(1-2), 140-151.
30. Golombek, M., Grott, M., Kargl, G., Andrade, J., Marshall, J., Warner, N., ... & Banerdt, W. B. (2018). Geology and physical properties investigations by the InSight lander. Space Science Reviews, 214(5), 1-52.
31. Golombek, M., Warner, N. H., Grant, J. A., Hauber, E., Ansan, V., Weitz, C. M., ... & Banerdt, W. B. (2020). Geology of the InSight landing site on Mars. Nature communications, 11(1), 1-11.
32. Pan, L., Quantin-Nataf, C., Tauzin, B., Michaut, C., Golombek, M., Lognonné, P., ... & Lucas, A. (2020). Crust stratigraphy and heterogeneities of the first kilometers at the dichotomy boundary in western Elysium Planitia and implications for InSight lander. Icarus, 338, 113511.
33. Baratoux, D., Samuel, H., Michaut, C., Toplis, M. J., Monnereau, M., Wieczorek, M., ... & Kurita, K. (2014). Petrological constraints on the density of the Martian crust. Journal of Geophysical Research: Planets, 119(7), 1707-1727.
34. Wilson, L. and Head, J. W. III (1994) Mars: Review and analysis of volcanic eruption theory and relationships to observed landforms. Rev. Geophys., 32, 221-263.
35. Christiansen, E. H., Best, M. G. and Radebaugh, J. (2022) The origin of magma on planetary bodies. In: T. K. P. Gregg, R. M. C. Lopes and S. A. Fagents (Eds.) Planetary Volcanism Across the Solar System (Elsevier, Amsterdam) pp. 235-270.
36. Taylor, G. J. (2013). The bulk composition of Mars. Geochemistry, 73(4), 401-420.

37. Black, B. A., & Manga, M. (2016). The eruptibility of magmas at Tharsis and Syrtis Major on Mars. Journal of Geophysical Research: Planets, 121(6), 944-964.
38. McCubbin, F. M., Nekvasil, H., Harrington, A. D., Elardo, S. M., Lindsley, D. H., J. Geophys. Res. – Planets, 113, E11013 (2008).
39. Gyalay, S., Nimmo, F., Plesa, A. C., Wieczorek, M., *Geophysical Research Letters*, **47**(16), e2020GL088653 (2020).
40. Manga, M. and Wright, V., 2021. No cryosphere-confined aquifer below InSight on Mars. Geophysical Research Letters, 48(8), p.e2021GL093127.
41. Clifford, S. M., Lasue, J., Heggy, E., Boisson, J., McGovern, P., & Max, M. D. (2010). Depth of the Martian cryosphere: Revised estimates and implications for the existence and detection of subpermafrost groundwater. Journal of Geophysical Research: Planets, 115(E7).
42. De Toffoli, B., Massironi, M., Mazzarini, F., & Bistacchi, A. (2021). Rheological and Mechanical Layering of the Crust underneath thumbprint terrains in Arcadia Planitia, Mars. Journal of Geophysical Research: Planets, 126(11), e2021JE007007.
43. Broquet, A., Wieczorek, M. A., *Journal of Geophysical Research: Planets*, **124**(8), 2054-2086 (2019).
44. Gudkova, T. V., Stepanova, I. E., & Batov, A. V. (2020). Density anomalies in subsurface layers of mars: Model estimates for the site of the InSight mission seismometer. Solar System Research, 54(1), 15-19.
45. Andrews-Hanna, J.C., Zuber, M. T., and Banerdt, W. B., (2008). The Borealis Basin and the Martian crustal dichotomy, Nature, 453, 1212-1215.
46. Nimmo, F. and Tanaka, K., 2005. Early crustal evolution of Mars. Annu. Rev. Earth Planet. Sci., 33, pp.133-161.
47. Citron, R.I., Manga, M. and Hemingway, D.J., 2018. Timing of oceans on Mars from shoreline deformation. Nature, 555(7698), pp.643-646.
48. InSight Marsquake Service (2022). Mars Seismic Catalogue, InSight Mission; V11 2022-07-01. ETHZ, IPGP, JPL, ICL, Univ. Bristol. https://doi.org/10.12686/a17
49. InSight Mars SEIS Data Service (2019). InSight SEIS Data Bundle. PDS Geosciences (GEO) Node, doi: 10.17189/1517570.
50. InSight Mars SEIS Data Service (2019). SEIS raw data, InSight Mission. IPGP, JPL, CNES, ETHZ, ICL, MPS, ISAE-Supaero, LPG, MFSC. http://doi.org/10.18715/SEIS.INSIGHT.XB_2016.
51. Lognonné, P., Banerdt, W. B., Giardini, D., Pike, W. T., Christensen, U., Laudet, P., ... & Berenguer, J. L. (2019). SEIS: Insight's seismic experiment for internal structure of Mars. Space Science Reviews, 215(1), 1-170.
52. Horleston et al., (2022). The far side of Mars: two distant marsquakes detected by InSight, The Seismic Record, 2 (2): 88-99.
53. Charalambous, C., Stott, A. E., Pike, T., McClean, J. B., Warren, T., Spiga, A., ... & Banerdt, W. B. (2021). A comodulation analysis of atmospheric energy injection into the ground motion at InSight, Mars. Journal of Geophysical Research. Planets.
54. Scholz, J. R., Widmer-Schnidrig, R., Davis, P., Lognonné, P., Pinot, B., Garcia, R. F., ... & Banerdt, W. B. (2020). Detection, analysis, and removal of glitches from InSight's seismic data from Mars. Earth and Space Science, 7(11), e2020EA001317.
55. Park, J., Vernon III, F. L., and C. R. Lindberg, Frequency dependent polarization analysis of high-frequency seismograms. *Journal of Geophysical Research: Solid Earth*, 92 (B12), pp. 12664-12674 (1987).
56. Clinton, J. F., Ceylan, S., van Driel, M., Giardini, D., Stähler, S. C., Böse, M., ... & Stott, A.

E. (2021). The Marsquake catalogue from InSight, sols 0–478. Physics of the Earth and Planetary Interiors, 310, 106595.

57. Ceylan, S., Clinton, J. F., Giardini, D., Böse, M., Charalambous, C., Van Driel, M., ... & Perrin, C. (2021). Companion guide to the marsquake catalog from InSight, Sols 0–478: Data content and non-seismic events. Physics of the Earth and Planetary Interiors, 310, 106597.
58. Dahmen, N. L., Zenhäusern, G., Clinton, J. F., Giardini, D., Stähler, S. C., Ceylan, S., ... & Banerdt, W. B. (2021). Resonances and lander modes observed by insight on Mars (1–9 Hz). Bulletin of the Seismological Society of America, 111(6), 2924-2950.
59. Poppeliers C., and Preston L. 2019. The use of multiwavelets to quantify the uncertainty of single-station surface wave dispersion estimates, Seismol. Res. Lett. 90, no. 2A, 754–764, doi: https://doi.org/10.1785/0220180145.
60. Preston, L., Poppeliers, C., & Schodt, D. J. (2020). Seismic Characterization of the Nevada National Security Site Using Joint Body Wave, Surface Wave, and Gravity Inversion Seismic Characterization of the NNSS Using Joint Body Wave, Surface Wave, and Gravity Inversion. Bulletin of the Seismological Society of America, 110(1), 110-126.
61. Dziewonski, A., Bloch, S., & Landisman, M. (1969). A technique for the analysis of transient seismic signals. Bulletin of the seismological Society of America, 59(1), 427-444.
62. Meier, T., Dietrich, K., Stöckhert, B., & Harjes, H. P. (2004). One-dimensional models of shear wave velocity for the eastern Mediterranean obtained from the inversion of Rayleigh wave phase velocities and tectonic implications. Geophysical Journal International, 156(1), 45-58.
63. Levshin, A. L., Ritzwoller, M. H., & Resovsky, J. S. (1999). Source effects on surface wave group travel times and group velocity maps. Physics of the Earth and Planetary Interiors, 115(3-4), 293-312.
64. Laske, G., and Widmer-Schnidrig, R., (2015). Theories and Observations: Normal Mode and Surface Wave Observations. Treaties on Geophysics, http://dx.doi.org/10.1016/B978-0-444-53802-4.00003-8
65. Sambridge, Malcolm, and Klaus Mosegaard. “Monte Carlo Methods in Geophysical Inverse Problems.” *Reviews of Geophysics* 40, no. 3 (2002): 3-1-3–29. https://doi.org/10.1029/2000RG000089.
66. Jiang, Chengxin, Brandon Schmandt, Jamie Farrell, Fan Chi Lin, and Kevin M. Ward. “Seismically Anisotropic Magma Reservoirs Underlying Silicic Calderas.” *Geology* 46, no. 8 (2018): 727–30. https://doi.org/10.1130/G45104.1.
67. Kennett, B. L. N. (1991). The removal of free surface interactions from three-component seismograms. Geophysical Journal International, 104(1), 153-163.
68. Christensen, Nikolas I, and Walter D Mooney. “Seismic Velocity Structure and Composition of the Continental Crust: A Global View.” *Journal of Geophysical Research: Solid Earth* 100, no. B6 (1995): 9761–88.
69. Herrmann, Robert B. “Computer Programs in Seismology: An Evolving Tool for Instruction and Research.” *Seismological Research Letters* 84, no. 6 (2013): 1081–88. https://doi.org/10.1785/0220110096.
70. Hastings, W Keith. “Monte Carlo Sampling Methods Using Markov Chains and Their Applications.” *Biometrika* 57 (1970): 97–109.
71. Drilleau, M., Beucler, E., Mocquet, A., Verhoeven, O., Moebs, G., Burgos, G., ... & Vacher, P. (2013). A Bayesian approach to infer radial models of temperature and anisotropy in the transition zone from surface wave dispersion curves. Geophysical Journal International, 195(2), 1165-1183.
72. Drilleau, M., Samuel, H., Rivoldini, A., Panning, M., & Lognonné, P. (2021). Bayesian

inversion of the Martian structure using geodynamic constraints. Geophysical Journal International, 226(3), 1615-1644.
73. Birch, F. (1961). The velocity of compressional waves in rocks to 10 kilobars: 2. Journal of Geophysical Research, 66(7), 2199-2224.
74. Malinverno, A. (2002). Parsimonious Bayesian Markov chain Monte Carlo inversion in a nonlinear geophysical problem. Geophysical Journal International, 151(3), 675-688.
75. Gao, C., & Lekić, V. (2018). Consequences of parametrization choices in surface wave inversion: Insights from transdimensional Bayesian methods. Geophysical Journal International, 215(2), 1037-1063.
76. Masters, G., Woodhouse, J. H., & Freeman, G. (2011). Mineos v1. 0.2 [software], computational infrastructure for geodynamics. Available from: geodynamics. org, doi: NoDOI, url: https://geodynamics. org/cig/software/mineos.
77. Weidner, E., Beghein, C., Huang, Q., and Schmerr, N., 2021. Upper mantle radial anisotropy under the Indian Ocean from higher mode surface waves and a hierarchical transdismensional approach, Geophys. J. Int., 228, 78-101.
78. Koper, K.D., Wysession, M.E. & Wiens, D.A., 1999. Multimodal function optimization with a niching genetic algorithm: a seismological example, Bull. seism. Soc. Am., 89(4), 978–988.
79. Li, J., Chen, M., Koper, K.D., Zhou, T., Xi, Z., Li, S. & Li, G., 2021. FastTrip: a fast MPI-accelerated 1D triplication waveform inversion package for constraining mantle transition zone discontinuities, Seismol. Res. Lett., 92(4), 2647–2656.
80. Dou, S., & Ajo-Franklin, J. B. (2014). Full-wavefield inversion of surface waves for mapping embedded low-velocity zones in permafrost. Geophysics, 79(6), EN107-EN124.
81. Schmerr, N. C., Banks, M. E., & Daubar, I. J. (2019). The seismic signatures of recently formed impact craters on Mars. Journal of Geophysical Research: Planets, 124(11), 3063-3081.
82. Maupin, V. (2017). 3-D sensitivity kernels of the Rayleigh wave ellipticity. Geophysical Journal International, 211(1), 107-119.
83. Lin, F. C., Tsai, V. C., & Schmandt, B. (2014). 3-D crustal structure of the western United States: application of Rayleigh-wave ellipticity extracted from noise cross-correlations. Geophysical Journal International, 198(2), 656-670.
84. Park, J., Lindberg, C. R., & Vernon III, F. L. (1987). Multitaper spectral analysis of high-frequency seismograms. Journal of Geophysical Research: Solid Earth, 92(B12), 12675-12684.
85. Tanimoto, T., & Rivera, L. (2008). The ZH ratio method for long-period seismic data: sensitivity kernels and observational techniques. Geophysical Journal International, 172(1), 187-198.
86. Dahlen, F. A., Tromp, J. (1998). Theoretical Global Seismology, Princeton University Press, Princeton, New Jersey
87. Ligorria, J. P., & Ammon, C. J., Iterative deconvolution and receiver-function estimation. Bulletin of the seismological Society of America , 89(5):1395–1400, 1999.
88. Kind, R., Kosarev, G. L., & Petersen, N. V. (1995). Receiver functions at the stations of the German Regional Seismic Network (GRSN). Geophysical Journal International, 121(1), 191-202.
89. Te Wu, T. (1966). The effect of inclusion shape on the elastic moduli of a two-phase material. International Journal of solids and structures, 2(1), 1-8.
90. Toksöz, M. N., Cheng, C. H., & Timur, A. (1976). Velocities of seismic waves in porous rocks. Geophysics, 41(4), 621-645.
91. Heap, M. J. (2019). P-and S-wave velocity of dry, water-saturated, and frozen basalt:

Implications for the interpretation of Martian seismic data. Icarus, 330, 11-15.

Acknowledgments:

This paper is InSight contribution number 266. The authors acknowledge the NASA, the CNES, their partner agencies and Institutions (UKSA, SSO, DLR, JPL, IPGP-CNRS, ETHZ, IC, and MPS-MPG) and the flight operations team at JPL, SISMOC, MSDS, IRIS-DMC, and PDS for providing the SEED SEIS data. We acknowledge the thorough and thoughtful reviews from the editor and three anonymous reviewers which greatly improved the manuscript. **Fundings:** ND, CD, GZ, and SCS would like to acknowledge support from ETH through the ETH+ funding scheme (ETH+02 19-1: \Planet Mars"). NS and VLacknowledge support from NASA PSP grant 80NSSC18K1628. CB and JL were supported by NASA InSight PSP grant #80NSSC18K1679. The French co-authors acknowledge the funding support provided by Centre national d'études spatiales (CNES) and the Agence Nationale de la Recherche (ANR-19-CE31-0008-08 MAGIS) for SEIS operation and SEIS Science analysis. Numerical computations of McMC Approach 2 were performed on the S-CAPAD/DANTE platform (IPGP, France) and using the HPC resources of IDRIS under the allocation A0110413017 made by GENCI. AH is funded by the UKSA under grant numbers ST/R002096/1 and ST/W002523/1. IJD was supported by NASA InSight PSP grant 80NSSC20K0971. A portion of this work was supported by the InSight Project at the Jet Propulsion Laboratory, California Institute of Technology, under a contract with the National Aeronautics and Space Administration. **Author contribution:** DK, SC, DG, VL, PL, CB, EB, JC, AK, BK, JL, MS, SCS, and ES, analyzed the seismic data and contributed in detection and identification of the surface wave arrivals. DK, VL, CB, MD, RJ, BK, JL, RM, HS, and EW performed the inversions. CC and WTP performed the comulation analysis. SCS performed the analysis on ray tracing. DK performed waveform simulations. SC, BK, and ZX performed the H/V analysis. DK, CD, and BK performed the receiver function analysis. Review of the continuous data and detection of seismic events was done by DK, SC, CC, JC, CD, SCS, ND, AH, TK, MP, and GZ. DK, WBB, SC, DG, VL, PL, CB, JC, MG, AK, BK, JL, RM, NS, SCS, MW, AB, TG, SK, SMM, FN, ACP, IES, and MPP participated and contributed to the interpretation of the results. DK wrote the main paper with contribution from DG, and VL. DK, WBB, SC, VL, CB, JC, MG, AK, BK, JL, WTP, RM, NS, SCS, MS, ES, MW, EB, PD, QH, SK, SMM, FN, ACP, and RG edited the main text and supplementary materials. S1094b and S1000a impact analysis and discussion are contributed from DG, PL, JC, SCS, AH, IJD, BF, RG, and LP. The InSight mission is managed by WBB, and MPP. The SEIS instrument development was led by PL, DG, WTP, and WBB. **Competing interests:** The authors declare that they have no competing interests. **Data and materials availability:** The InSight event catalogue (*48*) and waveform data are available from the IRIS-DMC, NASA-PDS (*49*) and IPGP data center (*50*).

Supplementary Materials

Materials and Methods

Supplementary Text

Figs. S1 to S22

References (*51–91*)

Science
AAAS

Supplementary Materials for

Surface Waves and Crustal Structure on Mars

D. Kim, Banerdt, W. B., Ceylan, S., Giardini, D., Lekic, V., Lognonné, P., Beghein, C., Beucler, E., Carrasco, S., Charalambous, C., Clinton, J., Drilleau, M., Durán, C., Golombek, M., Joshi, R., Khan, A., Knapmeyer-Endrun, B., Li, J., Maguire, R., Pike, W. T., Samuel, H., Schimmel, M., Schmerr, N., Stähler, S., Stutzmann, E., Wieczorek, M., Xu, Z., Batov, A., Bozdag, E., Dahmen, N., Davis, P., Gudkova, T., Horleston, A., Huang, Q., Kawamura, T., King, S., McLennan, S., Nimmo, F., Plasman, M., Plesa, A. C., Stepanova, I. E., Weidner, E., Zenhäusern, G., Daubar, I., Fernando, B., Garcia, R., Posiolova, L. V., Panning, M.

Correspondence to: doyeon.kim@erdw.ethz.ch

This PDF file includes:

Materials and Methods

Identification of the minor-arc Rayleigh waves in S1094b impact

We use the seismic recording of S1094b and rotate the 20 samples per second (sps) UVW channels from the Very Broad Band (VBB) sensor of the Seismic Experiment for Interior Structure (SEIS; *51*) to ZNE (Fig. S1-S2). MQS identified S1094b during the routine initial data monitoring via daily spectrograms (*52*). It is the fifth largest seismic event in terms of amplitude, and clearly visible above the noise even though it occurred during a windy afternoon. The P-arrival is clear both in the time and spectral domains and has been assigned a picking uncertainty of ±1 s. The S-arrival, on the other hand, is emergent and it is difficult to identify a clear phase onset (Fig. S1A-B). The MQS pick was made in the time domain guided by spectrograms, and the pick uncertainty is ±20s. Using the differential S-P times and the recent set of radial martian models (*11*), the event was located at a distance of ~60 (±6) degrees. Polarization analysis with particle motion hodograms indicated a back azimuth of 40 (-9, + 18) degrees. The event has a moment magnitude of Mw 4.0±0.2 computed from the plateau of displacement spectra at frequencies below 1 Hz (*52*).

The minor-arc Rayleigh wave (R1) arrival shows substantially stronger amplitude in the 8-15 s period range and is observed in the S-wave coda, 800 s after the P arrival in the vertical-component spectrogram (Fig. S1C). Its frequency content is considerably lower than that of the direct P and S arrivals as well as that of the highly scattered seismic energy present in the coda window. Throughout our analysis window of -300 and 1800 s from the P arrival, we do not observe signals with similar frequency content in the transverse component spectrogram (Fig. S1C). Because this seismic event occurred during the late afternoon when we typically observe strong winds, we conduct a comodulation analysis of the potential wind injection during the event (Fig. S3-S5; *53*; see Assessing Environmental Noise section). By analyzing the glitch-removed seismograms, we also confirm our seismic analysis is not affected by glitches (*54*). A set of narrow frequency bands with center periods between 3-30 s are used to construct time domain envelopes of the vertical-component seismogram (Fig. S1D). We observe dispersion during the signal duration of this anomalous seismic arrival in the 8-15 s period range.

Identification of the major-arc Rayleigh waves in S1094b impact

The major-arc Rayleigh wave (R2) arrival is weaker and seen at about 75 minutes after the R1 signal (Fig. S2A). The frequency content of R2 is comparable to that of the R1 signal and we observe both dispersion and elliptically polarized energy in the vertical plane in the 6-12 s period range (Fig. S2B). Injection of wind noise in the R2 analysis window is evident (see Assessing Environmental Noise section), which was not the case for R1. Due to low signal-to-noise ratios, the direction of propagation and particle motion of this arrival are unclear. Therefore, the identification of R2 is suggestive though not definitive. We find no evidence for the arrival of surface wave overtones, nor multi-orbiting Rayleigh waves in the S1094b waveforms.

Frequency-dependent polarization and back azimuth analysis

We conduct frequency-dependent polarization analysis (FDPA; *55*) on the S1094b waveforms to investigate the particle motion of R1 and R2 arrivals. First, we compute the S-transform of three-component event waveforms and compute a 3x3 cross-spectral covariance matrix in 90% overlapping time windows whose duration varies inversely with frequency. The relative sizes of the eigenvalues of this covariance matrix are related to the degree of polarization of the particle motion, while the complex-valued components of the eigenvectors describe the particle motion ellipsoid in each time-frequency window (*55*). This method has been previously implemented to extract seismic signals that are strongly linearly-polarized in vertical and horizontal directions, and

successfully identified the core-reflected ScS phases on Mars (*11*). To highlight elliptically-polarized signals in S1094b waveforms, representative of Rayleigh waves, we combine polarization attributes summarized in Table S2-1 of (*11*) and define a metric emphasizing vertically elliptical motion (VEM). We confirm the particle motion associated with R1 and R2 is strongly elliptically-polarized in the vertical plane and their average VEM across the 8-15 s frequency range are high (Fig. S1E and S2D). Notably, the average VEM value reaches its maximum during the signal duration of R1. The corresponding VEM within the analysis window of R2 is noisier but similarly reaches to the maximum. Other VEM maxima observed within our analysis window could result from long-period wind noise (*16*), consistent with the comodulation analysis of the potential wind injection during the event (Fig. S3A).

To estimate the back azimuth of the R1 and R2 arrivals, we take advantage of the fact that Rayleigh waves would show a ~90° phase shift between vertical and radial component data (Fig. S6). We perform a grid-search to find back azimuth values that maximize correlation between the radial waveform and the Hilbert transform of the vertical component waveforms computed for a 50 s long moving window. The back azimuth estimates suggest that the R1 arrival is propagating dominantly with retrograde particle motion close to 51° northeast, consistent with the estimate from the polarization of the direct P-wave. The particle motion hodograms derived from the estimated 51° back azimuth verify that the elliptically polarized seismic energy associated with R1 arrival is propagating dominantly with retrograde particle motion within the 8-15 s period range (Fig. S6B). No optimal back azimuth could be determined for the R2 arrival due to low signal-to-noise ratio of the data therefore the identification of R2 is not definitive (Fig. S6).

Assessing Environmental Noise Injection

The wind and pressure sensors were not recording during the seismic event windows discussed in this paper. Comodulation analysis was applied to the seismic signal to predict the power injected by atmospheric disturbances during the arrival of R1 (Fig. S3). The comodulation approach has shown to be particularly successful in identifying seismic energy that is in excess of the expected noise injected from the local weather (*52, 56, 57*). In the absence of wind-speed or pressure data, which are no longer taken due to power constraints, the excitation of weather-sensitive lander modes at 4 Hz and 6.3 Hz has proven an effective atmospheric proxy in estimating this injection on Mars (*53*, *58*). Using the variance and mean of the 6.3 Hz lander resonance together with available wind data from the neighboring sols (sols 1096, 1098, and 1099), the wind speed and direction during S1094b event are predicted and validated (Fig. S5) as similarly done in (*53*). The predicted wind speed during the main energy packets of the P- and S-waves is 11 ± 2 m/s, with transient peaks reaching up to 15 m/s. As the energy slowly dissipates, the wind speed slowly decreases to an average of 7–8 m/s. The direction of wind during the event is predicted to be 100 ± 20° (i.e., predominantly from east to west) which is largely different from the back azimuth of the impact crater (*20*). The wind direction slowly decreases to ~80° as the energy dissipates. Substantial excess seismic power, here taken as the sum of the signal variance in all three axes, is observed during the identified R1 arrival in passbands centered at periods of 9.4 s and 13.2 s against the expected atmosphere-driven noise (Fig. S3). Below 15 s, long-period wind noise dominates, and the strength of seismic signal becomes much weaker than both lander-mode estimates. This long-period signal corresponds to a predominantly horizontal particle motion, as expected to result from the wind (Fig. S6B). See (*16*) for the detailed characteristics of the wind-generated signal recorded by SEIS. Similar analysis is done for the data during the arrival of R2 (Fig. S4). Notably, broadband environmental injection starts to interfere with R2 signal at 00:13:00 UTC on Dec 25, 2021, so we do not extend our analysis of R2 arrival beyond this time.

Surface Wave Dispersion Measurements

To make group velocity dispersion measurements with the identified R1 and R2 arrivals, we use a single-station approach using a multiwavelet transformation (*59*). Because the wavelet transform optimizes the trade-off between time and frequency resolution compared to typical narrow-band filtering, this method achieves stable, higher resolution measurements along with robust error estimates (*60*). Here, we use 10 mutually orthogonal wavelet pairs to compute 10 dispersion estimates across the 6-18 s period range of the vertical component waveform (Fig. S7). The mean and standard deviation are drawn from 10 pairs of measurements enabling us to determine that measurements in the 8-15 s and 6-12 s period ranges are robust and have minimal wind contamination during the R1 and R2 arrivals, respectively (green box, Fig. S7A-B).

We validate our measurements against those obtained using the conventional narrow-band filter bank approach. We applied the multiple filter technique (MFT; *61*) as implemented by (*62*) to periods of 5 s and longer. After testing different values, we used a Gaussian width factor of 16 for narrow filter-bands. The dispersion curve was determined by tracing the maximum energy at each frequency in a time window between 800 and 860 s after the MQS P-arrival for R1, and between 5240 and 5300 s for R2 (blue curves, Fig. S7A-B). Both R1 and R2 measurements from MFT are within the uncertainty ranges of those from the wavelet transformation approach, and the maximum difference is less than 0.02 km/s.

Group velocity measurements have two advantages over phase velocity measurements at the periods considered: (i) they do not require source phase to be calculated and corrected (*63*), (ii) they suffer less from cycle skipping (*64*). On Mars, phase velocity measurement is much more challenging to make than on Earth because estimating the initial phase is much harder in the absence of constraints on the source depth and mechanism. Furthermore, we lack both a good understanding of lateral variations in structure and phase velocity measurements at long period (e.g., 100 – 150 s) that could be used to eliminate cycle-skipping errors at relatively short periods (<15 s) of our surface wave signals. Whole cycle ambiguity of phase velocity measurements implies that multiple phase velocity dispersion curves could be compatible with observations (Fig. S7C); therefore, we decided not to use phase velocity measurements to perform the inversion at this stage.

McMC Inversion of surface wave dispersion data

McMC Approach 1:

We invert group velocity measurements made on R1 between 8 – 15 s using a Markov chain Monte Carlo (McMC) approach (*65-66*), in which we parameterize Vs profiles using 8 B-spline functions overlying a constant velocity layer. The depth to the constant velocity layer is allowed to vary between 30 – 60 km. We assume an average V_P/V_S ratio of 1.81 estimated for the upper crust beneath *InSight* using a free surface transform matrix (FST, *67*) using the five high quality marsquakes analyzed in *9*. The scaling between V_P and density is employed based on (*68*). We predict the group velocity dispersion curve g_{pred} for a proposed model **m** using the Computer Programs in Seismology software package (*69*). In the McMC inversion, the model space, defined by a uniform a priori distribution, is sampled using the Metropolis-Hastings algorithm (*70*). In each iteration a model **m** is accepted or rejected based on the likelihood function (Eq. S1),

$$P = \exp\left(\frac{-\varphi(\mathbf{m})}{2}\right)$$

Equation S1.

where P is the probability and φ is the misfit function, defined as $\varphi(\mathbf{m}) = \sum \frac{(g_{obs} - g_{pred})^2}{\sigma^2}$ (i.e. the χ^2 misfit). Following a burn-in period of 1 million iterations, the McMC provides samples from the posterior distribution; when visualizing the posterior, we plot the best fitting 10,000 accepted models. We varied both the assumed *a priori* distribution and number of McMC iterations to ensure that our final model is not biased by these choices. Group velocity kernels calculated using the mean posterior velocity model (Fig. S8A) show that the sensitivity is weak at depths shallower than 5 km, which is reflected in the large posterior model uncertainties at shallowest depths (inset, Fig. 2C). Additionally, the longest periods considered in this inversion are only weakly sensitive to structure near 30 – 35 km depth and below. Fig. S8B shows the predicted group velocity dispersion for a suite of models in (*11*) where the crust below the *InSight* lander is constrained by the receiver function (RF) analysis (*7*). Those predictions based on the entire set of 3-layer models in (*7*) are shown in Fig. S8C. In general, the observed group velocity of both R1 and R2 is larger than expected, indicating that the Elysium Planitia may have slower than average crustal velocities.

McMC Approach 2:

To assess the robustness of the estimate of the posterior distribution on Vs profiles, we performed a second inversion in which the V_S profiles are parameterized using Bézier curves (*71-72*). V_S in the crust is built using six Bézier points, which can vary within 1.5 - 4.5 km/s between the surface and 35 km depth, and within 3.0–4.5 km/s below 35 km depth. The Moho (*i.e.*, the seismic discontinuity between the crust and mantle) can be located between 35 and 45 km depth. In the shallow mantle (the V_S profile stops at 50 km depth), the V_S profile is constructed using two Bézier points, and the Vs values are allowed to vary between 4.0 and 5.0 km/s. The *a priori* V_S distribution is shown in Fig. S9A. As in the B-spline inversion method mentioned above, a V_P/V_S ratio of 1.81 is assumed. Density is deduced from a scaling relationship with V_P, using Birch's law (*73*). The forward problem is solved using the Computer Programs in Seismology software package (*69*), and the inverse problem is performed via a McMC method relying on the Metropolis-Hastings algorithm (*70*). To efficiently sample the parameter space, we divide the inversion scheme into two steps, as in (*74*). First, using a different starting model for each chain, we run 216 independent Markov chains in parallel over 100000 iterations. The best-fitting model is then determined for each chain and sorted in ascending order. The 72 best-fitting models are used as the starting model for the second step, for which 72 Markov chains are run over 60000 iterations. The first and second steps of this inversion procedure can be seen as the burn-in period and the stationary period, respectively. Because the McMC algorithm provides a series of dependent models, the correlation between the output models is reduced by picking one model every 54 models. The *a posteriori* V_S distribution shown in Fig. S9B is thus composed of 80000 models. We observe that the V_S distribution is in very good agreement with the one obtained with the B-spline inversion method described above (Fig. 2D). Fig. S9C shows that all the sampled models can fit the data within uncertainty bounds.

rj-McMC Approach 3:

To assess the extent to which assumptions about κ (V_P/V_S ratio) and fixed parameterization affect the retrieved posterior velocity distributions, we also utilize transdimensional Bayesian (TB) inference (*74*), implemented through the reversible jump McMC method, which can retrieve tighter constraints on crustal structure from surface wave data when the correct number of layers is not known a priori (*75*). Despite the parameterization in terms of Voronoi nuclei defining layers

with constant properties, the method is also capable of retrieving smoothly-varying velocity profiles, if those are required by the data. Because of the transdimensional formulation, no assumptions are made regarding the presence or depth of a Moho or any other discontinuity. In Fig. S10, we show the posterior distribution on Vs from a TB inversion of the R1 group velocity measurements, using the implementation described in (*75*), calculating group velocities, c_g, from the phase velocities, c_p, and their derivatives with frequency: $c_g = c_p/(1 - \partial lnc/\partial ln\omega)$. The posterior is synthesized from three rjMcMC chains, each running for 300,000 iterations, with a burn-in period of 100,000 iterations, which is discarded prior to sampling. Convergence is assessed following the approach of (*75*). Density is fixed to 2800 g/cm^3, while the prior distributions on Vs and κ are uniform in the 1.5-5.5 km/s and 1.6-1.9 range, respectively. The prior on the number of Voronoi nuclei and their depths are both uniform in the 1-50 and 0-150 km range, respectively. The standard deviation for all parameter perturbations is set at 10% of the parameter prior range. Forward modeling is carried out using the reflectivity method with flat layers. We can see that the profiles of V_S obtained through TB inversion are very similar to those obtained with the other, fixed-parameterization methods, which means that assumptions about the depth profile of κ do not bias our velocity inferences; indeed, the posterior on κ shows that our group velocity measurements, unsurprisingly, cannot provide any resolution of this parameter.

rj-McMC Approach 4:

We also performed a fully non-linear TB inversion with the same style of parameterization as in McMC Approach 3, but using MINEOS (*76*) for the forward modeling and only inverting for V_S. V_P and density are provided by a reference model, based on the RF analysis (*7*), as in (*77*). As shown by Approach 3, fixing V_P should not affect the results significantly. The inversion results are formed from 40 chains, each running for 50,000 iterations. The first 30,000 iterations are the burn-in period, after which the current model is saved every 53 iterations. Each model is allowed to be composed of 1-3 crustal layers and a mantle layer. The prior on the number of crustal layers is a uniform distribution of 1-3. The prior on V_S in crustal layers is a uniform distribution between 2 km/s and 4 km/s. The prior on V_S in the mantle layer is a uniform distribution between 4 km/s and 5 km/s. The prior on the depth of the Moho is a uniform distribution between 30 km and 40 km.

While there are no acceptable models in the posterior distribution with only one crustal layer (Fig. S11B-C), we find that both two- and three-layer crustal models are equally likely in the posterior. The models with two crustal layers have an intracrustal boundary at 11-13 km and a Moho between 32 km and 39 km (Fig. S11B). For three-layer crustal models, the shallower intracrustal discontinuity is at 11-17 km. There is no clear signal of the deeper intracrustal discontinuity, which means that the data could support equally well a gradual change in V_S with depth or a discontinuity (Fig. S11C). In both sets of models, we find an upper layer with V_S of approximately 3 km/s, and that V_S is larger than what was found in the RF study down to at least 20 km depth.

Niche Genetic Algorithm Approach 5:

We inverted the group velocity measurements of R1 between periods 8 – 15 s using a Niche Genetic Algorithm (*78-79*). The main difference between Niche Genetic Algorithm and other McMC approaches is that while searching for models with better behaviors (low misfits), Niche Genetic Algorithm also promote model diversity by applying a penalty term for similar models. Therefore, Niche Genetic Algorithm is suitable for inversion problems in geophysics where multiple local minima might exist.

In the model setup, we fixed the number of layers. We note that since the surface waves at the measured periods in current periods show little sensitivity at very shallow depths (i.e., less than 5 km, see Fig. S8A), we specifically allow the existence of a thin layer at this depth range. Specifically, the thickness of this first layer is a free parameter and can vary from 1 to 5 km during the inversion. The second layer is located at 11 – 20 km, and the third layer is located at 21 – 50 km. The exact depths for those three layers are free parameters. The search range for the S-wave velocities in the first and second layers are both 1.0 - 4.0 km/s. For the third layer, we enforce that its S-wave velocity must be greater than that of the previous layer, with an increase of 0.2 – 2.0 km/s. We also imposed that the S-wave velocity in the mantle (i.e., below the third layer) has to be greater than the speed of the crust, with an increase of 0.2 – 2.0 km/s. We note that the S-wave velocities within those three crustal layers are uniform (i.e., layered crustal models). The S-wave velocities in the deeper part (> 80 km) of the model are from (*11*). The V_P/V_S ratio is assumed to be 1.80 and the density/V_S ratio is assumed to be 0.8 (*7*).
We calculated the group velocity for each model using MINEOS (*76*). The misfit is defined as:

$$\chi = \sum_{t=8}^{15} exp\left(-\frac{(G_{obs(t)} - G_{syn(t)})^2}{2\sigma_{obs(t)}{}^2}\right)$$

Equation S2.

where G_{obs} and G_{syn} are the observed and synthetic group velocity at period *t*, and is the standard deviation of the observed group velocity. We have calculated 40,000 models during the entire inversion, and 8,000 of them are selected as acceptable models since their corresponding group velocity at each period is within one standard deviation of the measured group velocity. The acceptable models (Fig. S11A) show scattered distributions in the top 1 – 3 km and in the mantle (e.g., deeper than 30 km), which are consistent with the sensitivity kernels (Fig. S8A). The S-wave velocities in the second and third layers are concentrated at 3.2 ± 0.2 km/s and 3.4 ± 0.2 km/s, respectively. Both the mean and the uncertainty of the inverted models (with layered crustal setting) are compatible with the smoothed models derived from other inversion methods discussed above.

S1000a

S1000a is a peculiar event in the MQS catalog that closely resembles S1094b both in terms of its broad frequency content and comparable magnitude estimate. As briefly discussed in *20*, S1000a is also found to be an impact in origin based on the MARCI image taken between September 21-23, 2021. For more details of the S1000a event characteristics, see (*20*) and (*52*). Two distinct long-period arrivals, at ~20 s and ~30 s periods, are visible in the vertical component spectrogram of S1000a in the R1 group arrival time range predicted based on the posterior distribution in Fig. 2D (Fig. S12-S13). At the periods of 20 s and 30 s, the S1000a R1 group velocities would be primarily sensitivities to the 14 - 31.5 km and 21.5 - 48 km depth (considering 40% in cumulative kernel strength), respectively (Fig. S13F); this is deeper than the sensitivity of the higher-frequency R1 observed for S1094b. While R1 in S1094b shows clear polarization, the comparative strength of the environmental injection during the expected R1 window of S1000a prevents a definitive identification on the basis of polarization (Fig. S14). The back azimuth estimates suggest that the ~30 s arrival is propagating dominantly with retrograde particle motion close to 22°, which is slightly northward of the great circle path to the impact crater, which has a back azimuth of ~34°

(Fig. S13C-D). Based on the back azimuth of 34°, the ~20 s arrival also shows retrograde particle motion but we could not determine an optimized back azimuth for this arrival (S12C-D).

The presence of two distinct long-period arrivals, instead of a continuous curve tracing the dispersed Rayleigh wave has been reported in permafrost regions on Earth (*80*) where the uppermost few meters are frozen, but the ice melts deeper down, producing a pronounced low velocity zone. However, this type of structure would imply faster group velocities at higher frequencies which is the opposite of what we observe in S1000a data. While we observe very little group velocity difference for S1000a (~4%), the longer period arrival still travels at higher velocities. Therefore, we speculate our discontinuous dispersion is due to a combination of different frequencies associated with each arrival at the same time, increasing the amplitude, combined with noise and scattering effects rather than crustal structure in origin.

We measure two average group velocities at ~20 s and ~30 s periods (2.73 km/s and 2.83 km/s) (Fig. S13F) and invert for V_S structure based on the McMC Approach 1 (Fig. 2E). The inferred V_S structure using the S1000a group velocity measurements overlaps with our posterior V_S distribution based on group velocities of R1 for S1094b, while providing constraints in the lower crust to 40 km depth. If substantiated by further analysis, this suggests a surprising degree of similarity in crustal structure along these R1 paths.

Waveform Simulation

To explore the characteristics of R1 arrival in S1094 event, we use the reflectivity method to generate synthetic waveforms in two different types of crustal models: an average crustal model along the R1 path and the crustal model beneath the lander location. Below the crust, we fix the velocities to those used in (*11*). For each model, fifty random focal mechanisms are considered for sources at 20 and 60 km depth (gray, Fig. S15). Because S1094b is a confirmed impact (*20*), we also simulate synthetics for an isotropic explosion source at the surface for both models and compare the result with those computed for double-coupled sources at depth (red, Fig. S15). Often, impact waveform simulation is done using a vertical or inclined force rather than an isotropic source. Due to large similarity in radiation pattern between directed forces vs. isotropic sources (*81*) and invariable propagation physics of the generated seismic waves in those simulations, we do not expect substantial variations in the resulting synthetics. Furthermore, we are fundamentally limited to make robust estimation of the focal mechanism for S1094b with a single station. Therefore, we do not explore various types of source mechanisms related to this impact. We extract the pre-event noise from the S1094b event data and add it to our synthetics. Using vertical component synthetic waveforms, we compute envelopes in the frequency domain by averaging the power spectral density across the 8-15 s period range. Strong R1 arrivals observed for both models using various focal mechanisms of the shallower, 20 km depth source are no longer visible with the deeper 60 km depth source. Notably, the surface isotropic source generates the strongest amplitude of R1 for all cases being considered in the analysis. The S-transform vertical component spectrograms shown in Fig. S15C-D illustrate the substantial difference in timing, signal duration, frequency content, and existence of the higher modes between the average crustal model along the R1 path and at the lander constrained by the surface wave analysis in this study and RF analysis (*7*), respectively. We also note the relative amplitude of the R1 depends on the dispersion curve. For example, in case of little dispersion, the apparent amplitude of the surface waves is enhanced (Fig. S15C) compared to the one with strong dispersion (Fig. S15D). Our data is compatible with the former (c.f., Fig. S15C and S15E). Our current understanding of martian crustal scattering and the parameters associated with attenuation is fairly limited. Therefore, the R1 arrivals simulated in this section and their source depth dependency should be interpreted in a relative sense.

Rayleigh Wave H/V Ratio

H/V ratio is a characteristic property of the Rayleigh wave and represents the ratios of the amplitudes of radial and vertical components of Rayleigh wave particle motion at different frequencies. Compared to Rayleigh-wave phase/group velocity measurements, which are sensitive to the subsurface under the path between seismic source and station, the H/V ratio is dominantly sensitive to the subsurface near the station (*82*). Furthermore, the H/V ratio is sensitive to Vs at shallow depth (*83*).

We measure the H/V ratios from the vertical- and radial-component deglitched VBB velocity data (*54*), where the radial direction is 40 deg from North. We bandpass filter the data between 0.055 Hz and 0.2 Hz and then compute the amplitude spectrum ratios of the two components from 101 20-second-long time windows between 800 s and 850 s after the P-wave arrival (Fig. S1A). For the martian crustal velocity model from receiver function (*7*), the H/V ratio is sensitive to Vs in the first 10 km depth (Fig. S16A-B). Since H/V ratio and receiver function are both sensitive to the structure under station, the H/V ratio of the S1094b Rayleigh wave signal is close to the synthetic H/V ratio from the crustal model (Fig. S16C). Meanwhile, since the H/V measurement is not sensitive to the Vs along the path of S1094b, we do not incorporate the H/V into our inversion.

In order to check its variability, we computed the H/V amplitudes using different time lengths. Here, we obtained the H/V from the time window of the Rayleigh wave, i.e., between 2021-12-24 22:58:29.07 and 2021-12-24 22:59:19.07 UTC (50 s long). Using the rotated ZRT waveforms, we computed the Fourier spectrum using different time-window durations of 20, 25, 30 and 40 s length, with an 98% overlapping factor in all cases, in order to check the stability of the H/V. For each time window, the Fourier spectrum was smoothed using the multi-tapering method proposed by (*84*) and, for each frequency, the H/V is obtained as the ratio between the spectral power of the radial and the vertical components (*85*). In order to compare our observations with the proposed models for the martian crust, we computed the synthetic H/V of the Rayleigh wave for the crustal models proposed by (*7*), both with two and three layers, and this work (Fig. S17). The H/V of the Rayleigh wave lies roughly between 0.8 and 1, especially between 0.65 and 0.12 Hz, where the Rayleigh wave is easily identifiable. Given the short duration of the Rayleigh wave time-window, the fine shape of the H/V curve is not well constrained and is highly dependent on the parameters chosen for the computation of the H/V. A common feature among the different calculations is that no clear peaks or troughs are observed in the frequency range between 0.65 and 0.12 Hz, suggesting the absence of a sharp contrast in the crust. Considering the rough shape of the H/V measurements for the Rayleigh wave, the synthetic H/V response from the crustal models with layers (*7*) better correlates with our observations than that from this work without those layers.

Ray Tracing

In order to estimate the effect of lateral variations in crustal thickness on surface wave travel times, we generate group and phase velocity maps of the planet. This is done in 3 steps:

1. Based on gravimetric data, as described in (*23*), a crustal thickness map is produced by fixing the crustal thickness to 40 km at the *InSight* location and assuming a density contrast over the Moho. To account for possible material variation in the southern highlands, we repeat the analysis with an increased crustal density of 2850 kg/m^3 south of the dichotomy. This results in a map of crustal thickness computed for spherical harmonics up to degree 120. The thinnest crust obtained is 14 km in Hellas, the thickest is 80 km in Tharsis.

2. We vary the crustal model retrieved in the inversion by changing the Moho depth and scaling the velocity gradient within the crust linearly with the relative Moho variation (Fig. S18). The uppermost layer is not modified. This yields 10 new crustal profiles between 14 and 80 km Moho depth. We compute group and phase velocity curves for each profile and map them to the whole planet based on the crustal thickness map described in (*21*). Group velocities are predicted to vary between 2600 and 3600 m/s, with a global average of 2800 m/s, as found for R1.
3. Within each model, we use a kinematic ray tracer based on equations (16.185 and 16.186) from (*86)* to obtain propagation paths and travel times for R1 and R2 (Fig. S19).

The resulting travel times deviate by less than 1% between the great circle arc path and the ray theoretical path. Therefore, we conclude that lateral thickness variations that cannot be resolved by the gravimetric modeling in (*21*) are unlikely to strongly affect the arrival times of R1 and R2. We further find that the single outlier in group velocity in Hellas Planitia is enough to explain the difference in average group velocity between R1 and R2.

RF Analysis

In order to represent the local structure response, we compute P-to-s RF of event S1094b by deconvolving the direct phase (P-wave) from the converted phase (S-wave). To this end, we follow the processing scheme described in (*8)*. Waveforms of event S1094b are tapered and band-pass filtered between 2 s and 5 s, and then rotated to the ZRT-system on the basis of the estimated back-azimuth provided by the *InSight*'s Marsquake Service (MQS) and latter verified by the large impact crater in Amazonis Planitia. Afterwards, to further separate P- and S-wave energy, traces are rotated to the LQT-system, where the L component is aligned in the direction of P-wave propagation and Q in the direction of SV-wave displacement. Rotation is achieved via principal component analysis, minimizing the energy on the radial component in a 30 s time window around the P-wave arrival. To compute the P-to-s RF, we apply an iterative time-domain deconvolution (*87*), deconvolving source from the response waveform. To extract the source wavelet and the response trace, we trim the corresponding waveforms around the picked P-wave within a window from -10 s to +50 s. The final P-to-s RF of event S1094b is shown in Fig. S20A, and compared with the RFs of high-quality events obtained by (*8*). The S1094b RF shows two strong arrivals in the first 5 s that are broadly consistent with the ones observed for most of the events (~2.4 s and ~4.8 s). Furthermore, a weaker third arrival is observed ~7 s. As demonstrated by (*7-9*), the timing of the observed arrivals indicates that they are mainly sensitive to crustal structure. To ensure that information from many events are combined coherently, we stack the RFs into a single trace representative of the structure below the station and show it in Fig. S20A in red. Once again, we observe a good agreement in the three selected windows between the arrivals observed in the stacked trace and the ones observed in the RF of S1094b. Last, to illustrate the good coherency in the three selected windows among all events, including S1094b, we overlap all the waveforms and depict them in Fig. S20B.

We also conduct a comparison of receiver functions obtained by an independent approach. Fig. S21 shows a comparison of P-to-s RF of S1094b to those of known high-quality events previously employed to constrain the crustal structure at the *InSight* landing site by (*7*) and (*9*), i.e. S0173a, S0183a, S0235b, S0809a and S0820a. Four out of these five events are located in the Cerberus Fossae region, and all of them are located at a closer distance to *InSight* than S1094b. The RF for S0820a shows a high level of noise after about 10 s due to the arrival of the PP-phase

that is interfering with the P-to-S conversions following the direct P phase (*9*). RFs for all data were computed following the steps outlined in (*7*), method D: Data were first response corrected, then rotated to the ZNE system and filtered to enhance seismic signals by a Butterworth zero-phase bandpass of third order. The corner periods were 0.1 and 0.8 Hz in case of S0173a and S0235b, 0.3 and 0.8 Hz in case of S0183a, S0809a and S0820a, and 0.1 and 1 Hz in case of S1094b. Using the back-azimuth estimates from MQS, the data were rotated into the ZRT system. Then, polarization analysis by diagonalization of the coherence matrix of the P-wave onset was used to determine the incidence angle of the P-wave for further rotation to the LQT-system. A time-domain Wiener filter that transforms the P-wavetrain on the P-component into a band-limited spike was used to calculate the receiver functions by applying this filter to all three components (*88*). A free parameter here is the length of the deconvolution window. After several tests, window lengths of 40 s for S0173a, 28 s for S0183a, 33 s for S0235b, 44 s for S0809a, 49 s for S0820a and 64 s for S1094b were used. The spike is positioned at the centroid of the signal in each case. The damping factor also influences the shape of the resulting receiver functions. We aimed at using a low amount of damping, with values of 0.1 for S0173a and S0809a, 0.5 for S0235b, S0820a, and S1094b, and 1 for S0183a. The receiver function for S1094b shows two clear arrivals at 2.4 and 4.8 s that are very consistent with the other events, whereas the arrival at about 7.2 s is less clearly visible. These three arrivals are related to the crustal structure below the *InSight* landing site; specifically, the first arrival at 2.4 s that is very clear in the receiver function for S1094b is related to a discontinuity at about 10 km depth, whereas the second arrival at 4.8 s also relates to an interface at less than 30 km depth (*7*), i.e. both lie within the depth range where the Rayleigh waves analyzed here have good resolution.

Effect of Porosity on Seismic Velocity

To interpret the observed differences between the layered crustal structure right below the *InSight* lander (*6, 7*) and the structure inferred from surface wave group velocity inversion in this study in terms of porosity, we build on the modeling performed by (*40*). They used the equations for the self-consistent composite elastic moduli of a two-phase material with spherical inclusions as derived by (*89*) and (*90*) and the elastic parameters compiled by (*91*) to constrain the hydrology beneath *InSight* by comparing the S-wave velocities determined by (*6*) for the uppermost 10 km of the crust to modeled values depending on the porosity, aspect ratio of the pores, and the material filling the pores. The matrix is assumed to consist of basalt, based on the material observed at the surface in the landing region. However, as discussed in the main text, sedimentary material could also figure prominently in the crust below *InSight*. Here, we compare the values for CO_2-filled pores to the S-wave velocities of the top-most layer determined by (*7*), which broadly lie between 1.6 and 2.0 km/s (left, Fig. S22). The values are compatible for a porosity of 10% or larger and a low aspect ratio smaller than 0.1, which is compatible with basalt fractured due to repeated impacts. Transferring the trade-off curve between aspect ratio and porosity that is consistent with a velocity of 1.8 km/s to the case of basalt with ice-filled pores leads to velocities that are consistent with the values derived from surface wave inversions (right, Fig. S22). Water-filled pores, on the other hand, would lead to slightly lower S-wave velocities compared to the case with CO_2 filling (*40*), so they cannot adequately explain the observations.

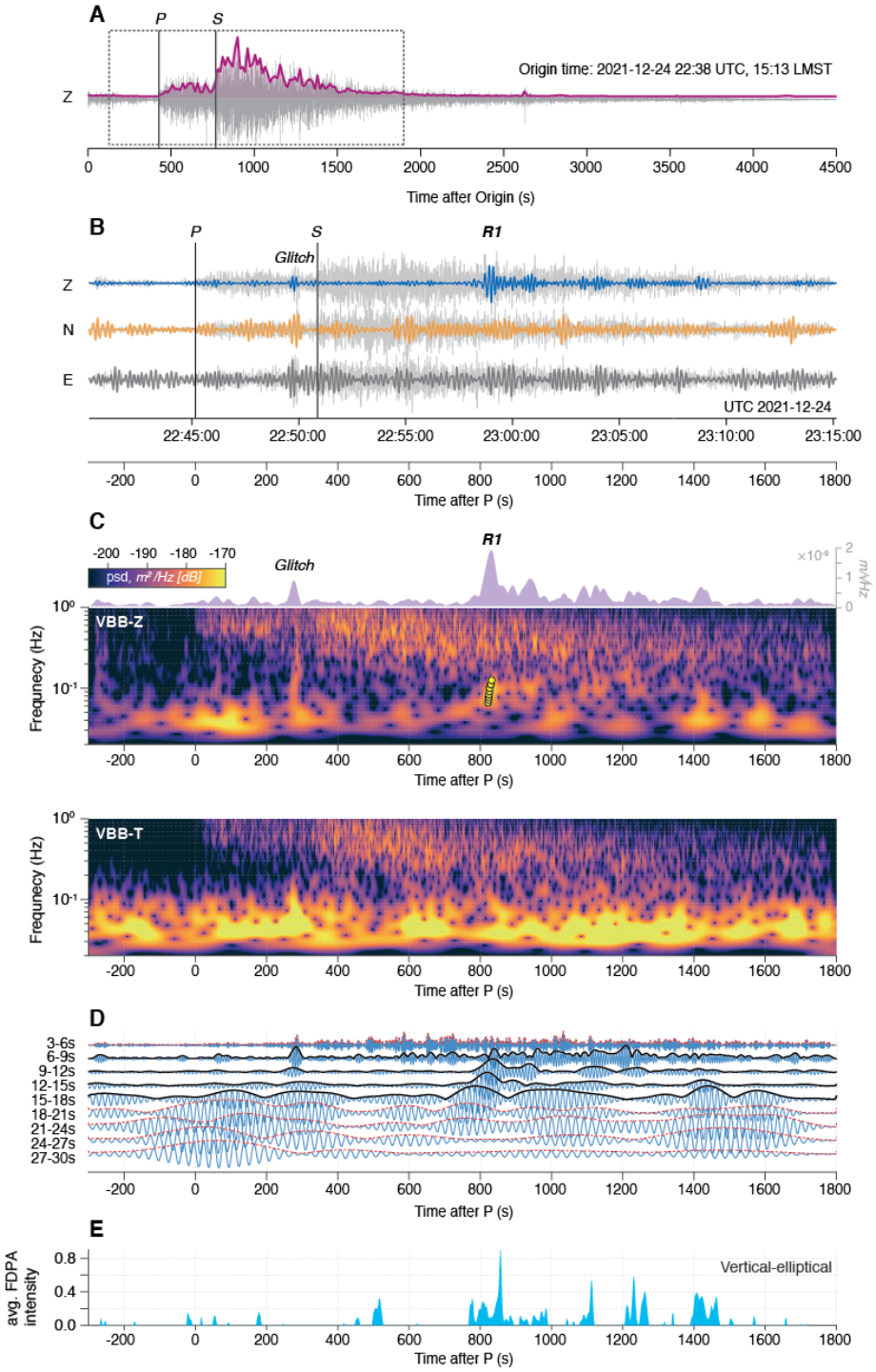

Figure S1. Summary of data processing of the R1 arrival. (**A**) Vertical component times series of event S1094b bandpass filtered between 1-10 s and derived spectral envelope. (**B**) Zoom-in of three-component seismograms bandpass filtered between 1-5 s (light gray) and 8-15 s (blue, orange, dark gray). Phase picks are shown by the black vertical lines. Pick uncertainties of P and S waves are ±1 s and ±20 s, respectively. (**C**) Vertical and transpose component S-transform spectrograms. The corresponding vertical envelope averaging the power spectral density across the 8-15 s period range is displayed at the top of the vertical spectrogram. Yellow dots in the

spectrogram denotes the R1 measurement shown in Fig. 2C. (**D**) Narrow-band filter banks and envelopes show dispersed signals observed 800 s after the P wave. Black and red envelopes indicate the signals associated with the surface waves and noise, respectively (**E**) Combined polarization metric averaged across 8-15 s (VEM) based on the FDPA.

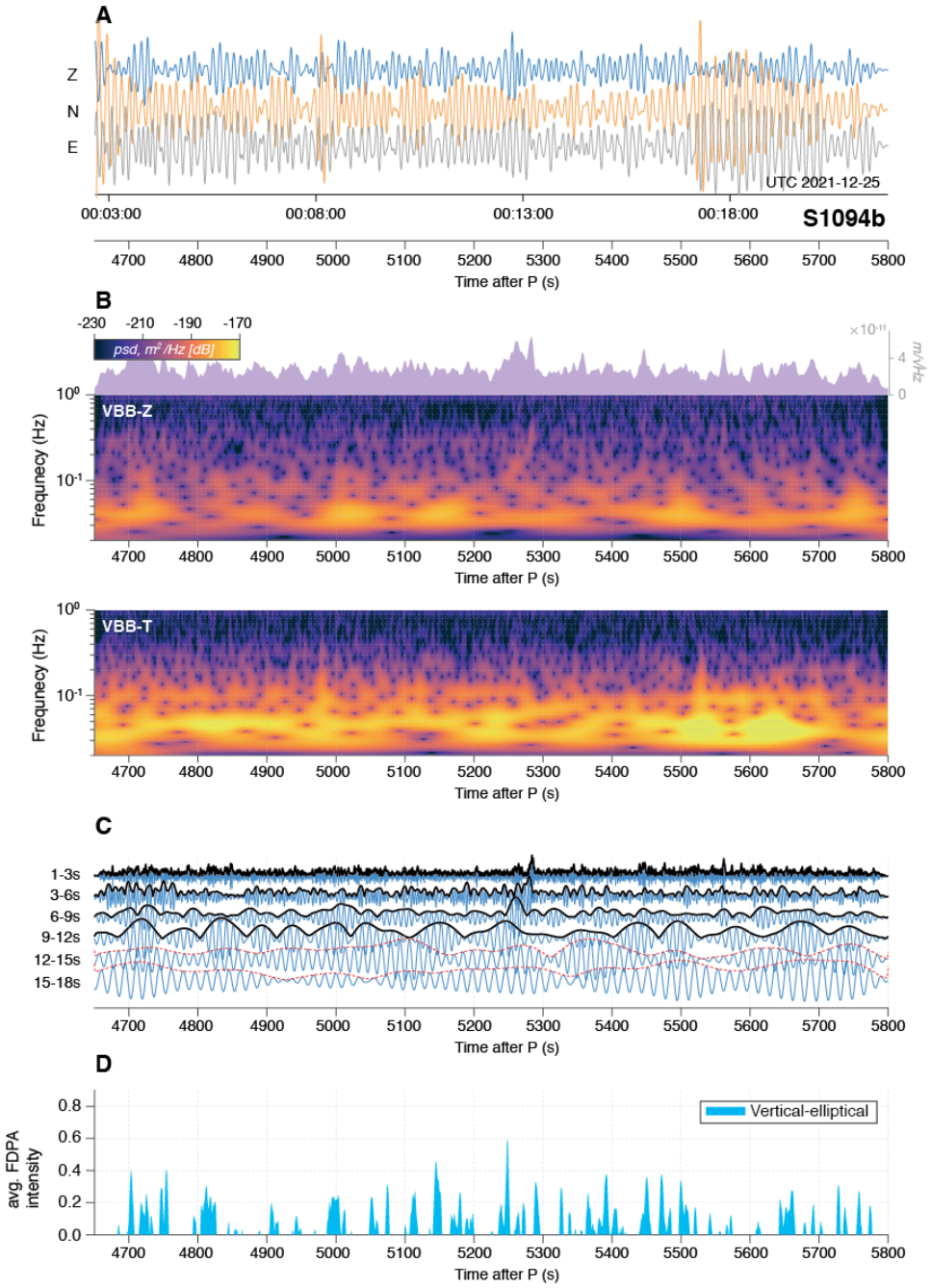

Figure S2. Summary of data processing of the R2 arrival. Details as Fig. S1 but for the signal associated with the R2 arrival. (**A**) Three-component seismograms of event S1094b bandpass filtered between 6-11 s. (**B**) Vertical and transpose component S-transform spectrograms. The corresponding vertical envelope averaging the power spectral density across the 6-11 s period range is displayed at the top of the vertical spectrogram. (**C**) Narrow-band filter banks and envelopes show dispersed signals observed ~5280 s after the P-wave. Black and red envelopes

indicate the signals associated with the surface waves and noise, respectively. (**D**) Combined polarization metric averaged across 6-11 s (VEM) based on the FDPA.

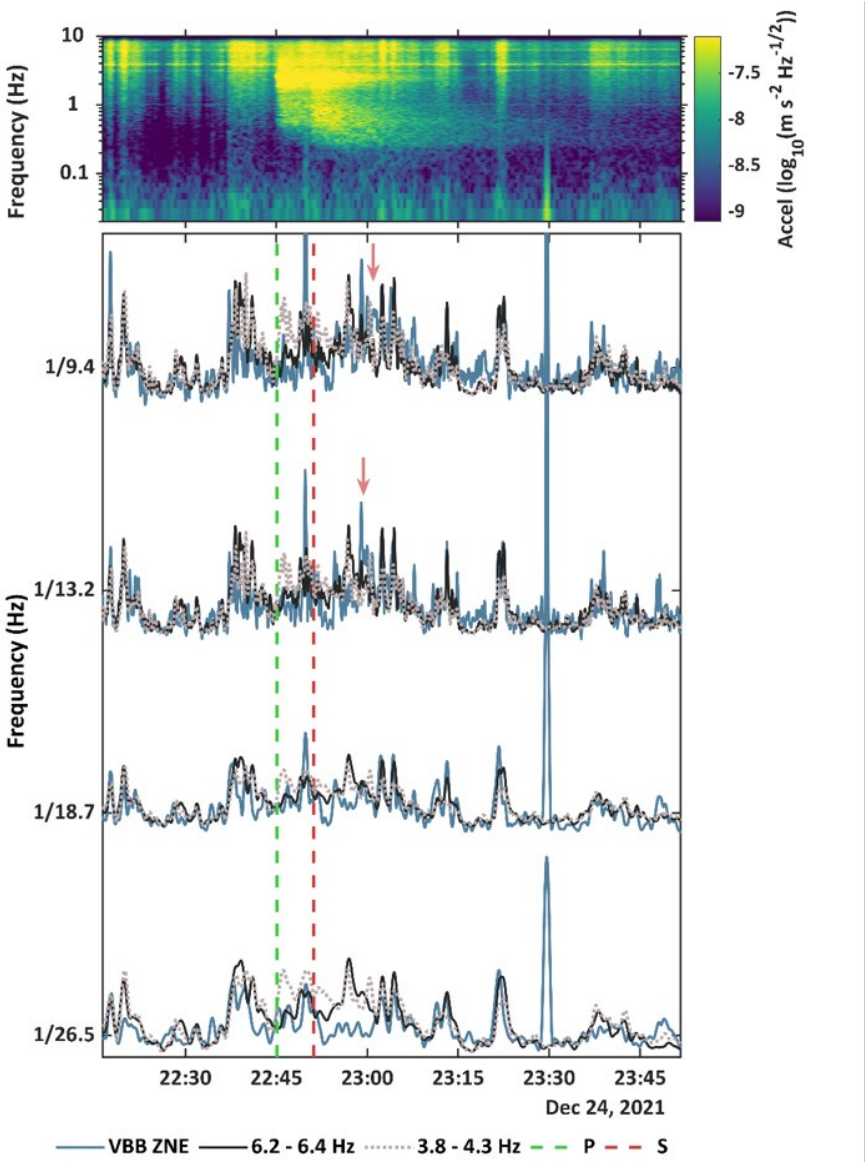

Figure S3. Comodulation analysis of the R1 arrival. The top figure shows the spectrogram of the total signal power in all three axes (ZNE) of VBB 20 sps, calculated using 100-s long hanning windows. The line traces show a comparison between the seismic and estimated atmospheric power of the signal. The total seismic signal power (solid teal) is in half- octave windows centered at 9.4, 13.2, 18.7 and 26.5 s periods. The atmospheric signal power of the weather-sensitive lander resonances at 4 (solid black) and 6.3 (dotted grey) Hz, variance- and mean-matched to the seismic signal in the window prior to the P-wave arrival. Where the seismic line trace is above the atmospheric line trace, the residual can be attributed to a seismic injection, with the R1 arrival indicated by the red arrows. P- and S-wave arrivals are marked by vertical green and red dashed lines respectively.

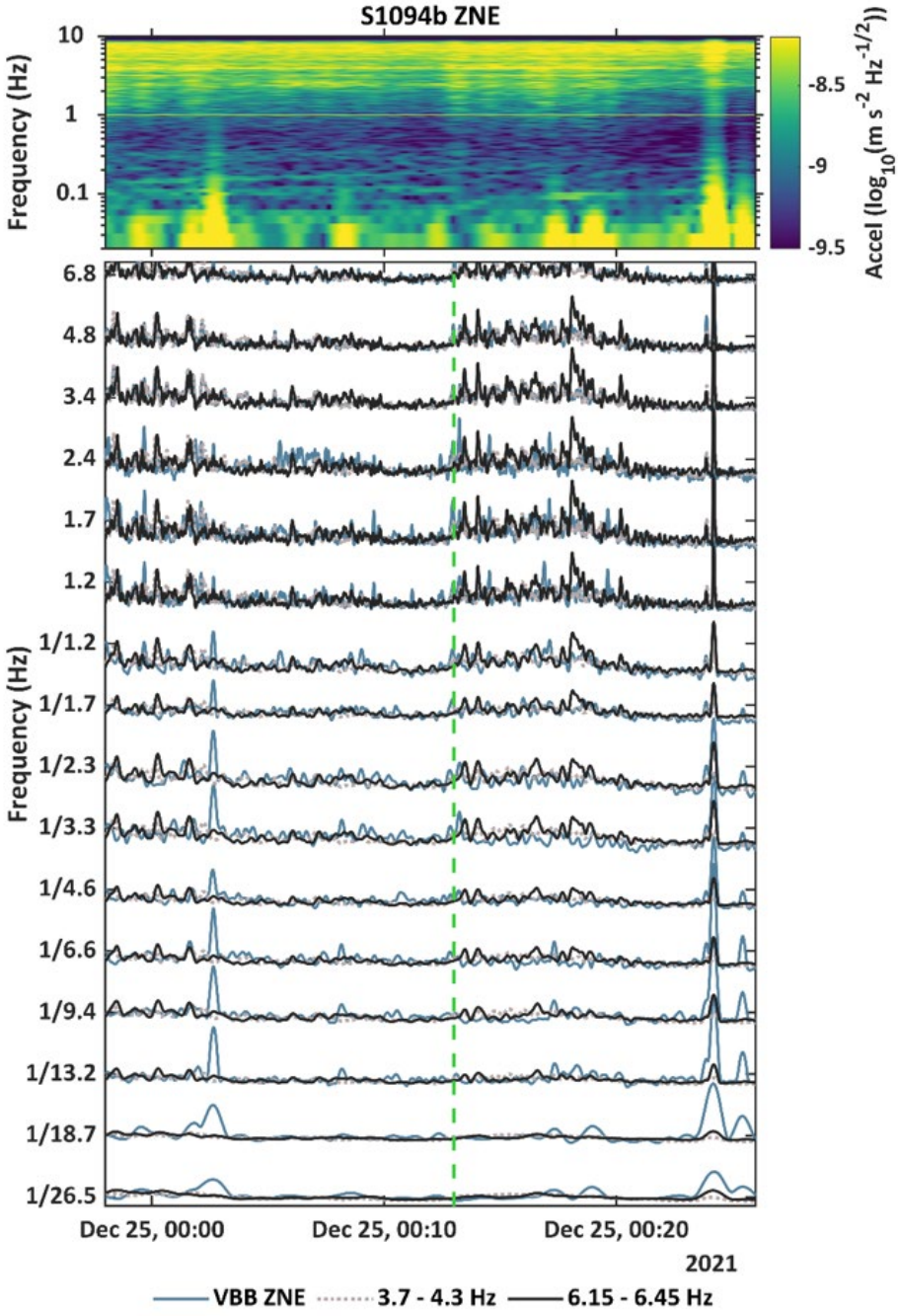

Figure S4. Comodulation analysis of the R2 arrival. Same as Fig. S3 but results on the analysis extended up to 6.8 Hz. Strong broadband environmental injection starts ~00:13:00 UTC on Dec 25, 2021 (green dashed line) therefore we do not extend our analysis / interpretation of R2 arrival beyond this time.

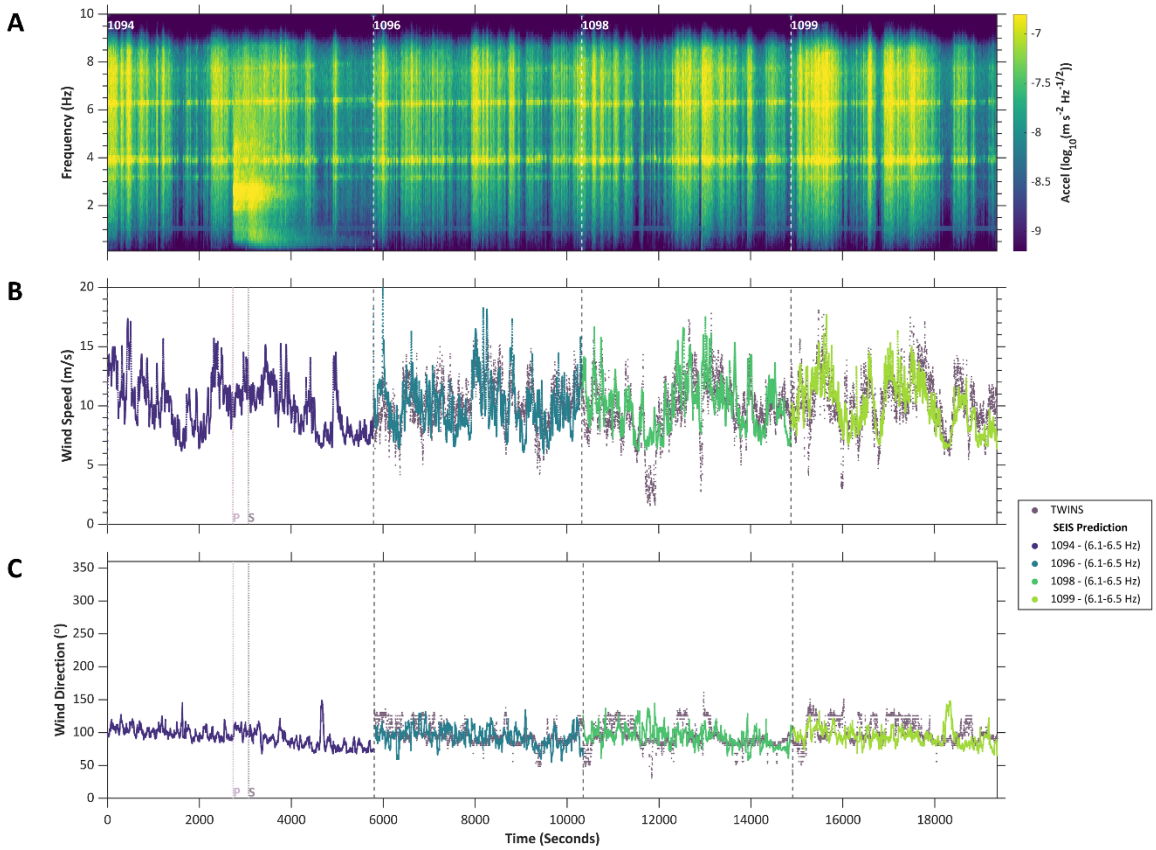

Figure S5. Characteristics of wind during S1094b. Estimations of wind speed and wind direction determined from SEIS data based on comodulation analysis of the atmospheric signal power at the 6.3 Hz lander resonance (*53*), as also shown in Fig. S3-S4. These estimates were validated with the same parameters by the match of the three nearest sols (1096, 1098 & 1099) that have wind data available at a similar time of occurrence, 14.30 – 16.30 Local Mean Solar Time (LMST). (**A**) Combined energy spectrograms for VBB ZNE 20 sps data for sol 1094 followed by spectrograms of sols 1096, 1098 and 1099 between 14.30-16.30 LMST. (**B**) Wind speed estimations (colored lines), including comparison against measured wind data (grey dots) from the three nearest sols that have TWINS data available. (**C**) Wind direction estimations (colored lines), including comparison against measured wind data (grey dots) from the three nearest sols that have TWINS data available.

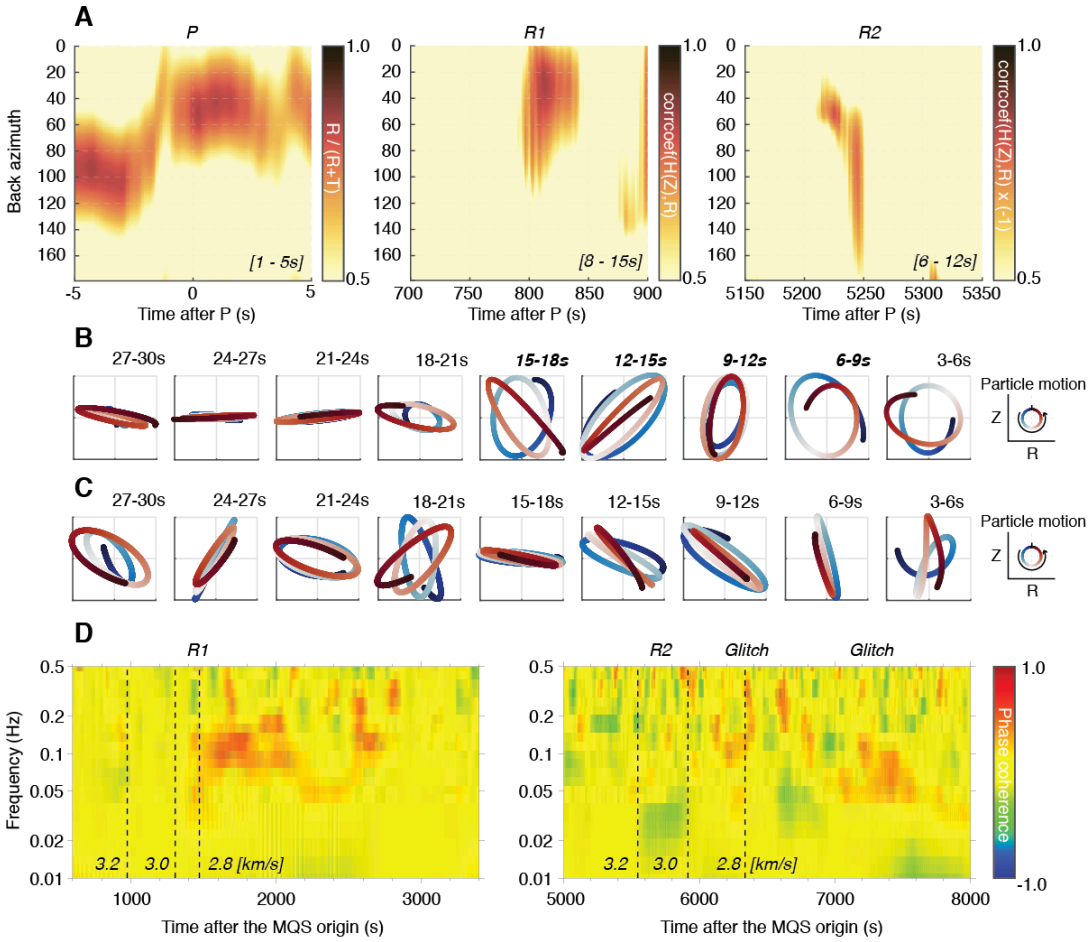

Figure S6. Back azimuth estimates and hodograms of S1094b. (**A**) The resulting back azimuth search of P, R1, and R2 arrivals in S1094b. The back azimuth estimates suggest that the propagation direction of the R1 arrival is consistent with the estimate from the polarization of the direct P wave. No optimal back azimuth is determined for the R2 arrival due to low signal-to-noise ratio of the data. (**B-C**) Hodograms constructed using vertical and radial component waveforms after rotating the raw horizontal components with 51° back azimuth. Retrograde particle motion of the R1 arrival is clearly visible between the 8-15 s period. As expected, the corresponding particle motion for R2 arrival is more complex. (**D**) Phase coherence of Hilbert transformed vertical component with radial component using 51° back azimuth. A positive correlation is expected for the R1 wavetrain while a negative correlation is expected for the R2 arriving from the opposite direction.

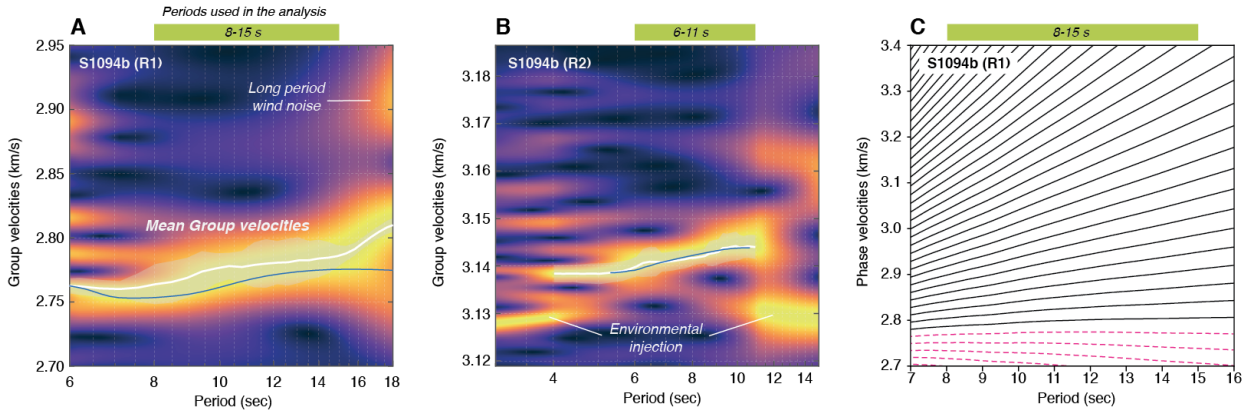

Figure S7. Summary of the group velocity measurements and predictions. (**A**) Mean group velocity measurements of the R1 and (**B**) R2 arrivals and their uncertainties based on a multiwavelet approach described above. Green box above each panel indicates the period used in the analysis. Blue curves are those measurements from using the MFT approach. (**C**) Phase velocity estimates for the R1 arrival and the non-uniqueness. The phase velocities are estimated assuming a zero initial phase in the source based on our group velocity measurement in S7A. The solid black curves are phase velocity dispersion curves with velocity larger than the group velocity, while the dashed black curves are phase velocity dispersion curves with velocity smaller than the group velocity.

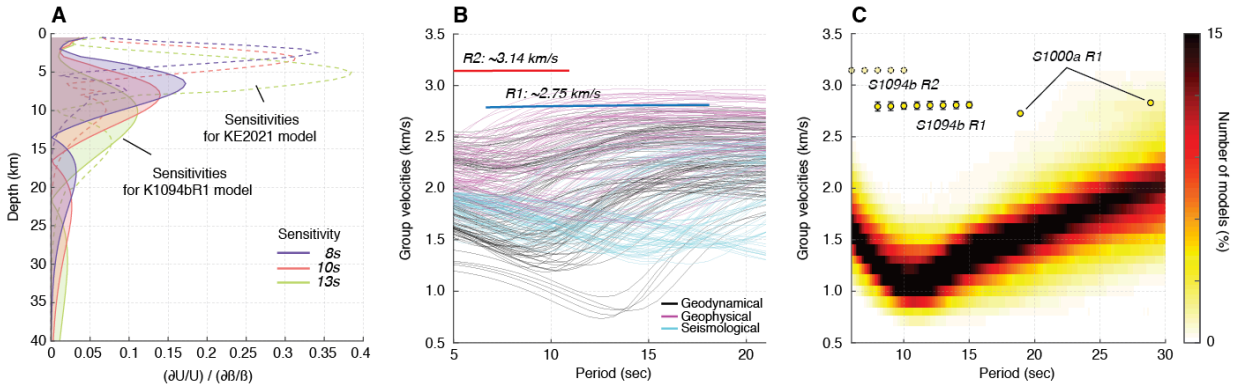

Figure S8. (**A**) Depth sensitivity kernels (shaded) computed for 8 s, 10 s, and 13 s based on the average crustal model (K1094bR1) inverted using the R1 measurements shown in S7A. The corresponding kernels computed for the 3-layer crustal model beneath the station (denoted as KE2021) are shown as dashed curves. (**B**) Comparison of the group velocity measurements and predictions made using 100 randomly selected best-fitting models in (*11*). See details in (*11*) for three types of parameterization strategies (geodynamical, geophysical, and seismological) used for constructing those models. (**C**) Comparison of the group velocity measurements and predictions made using 20,000 3-layer models constrained by the receiver function study in (*7*).

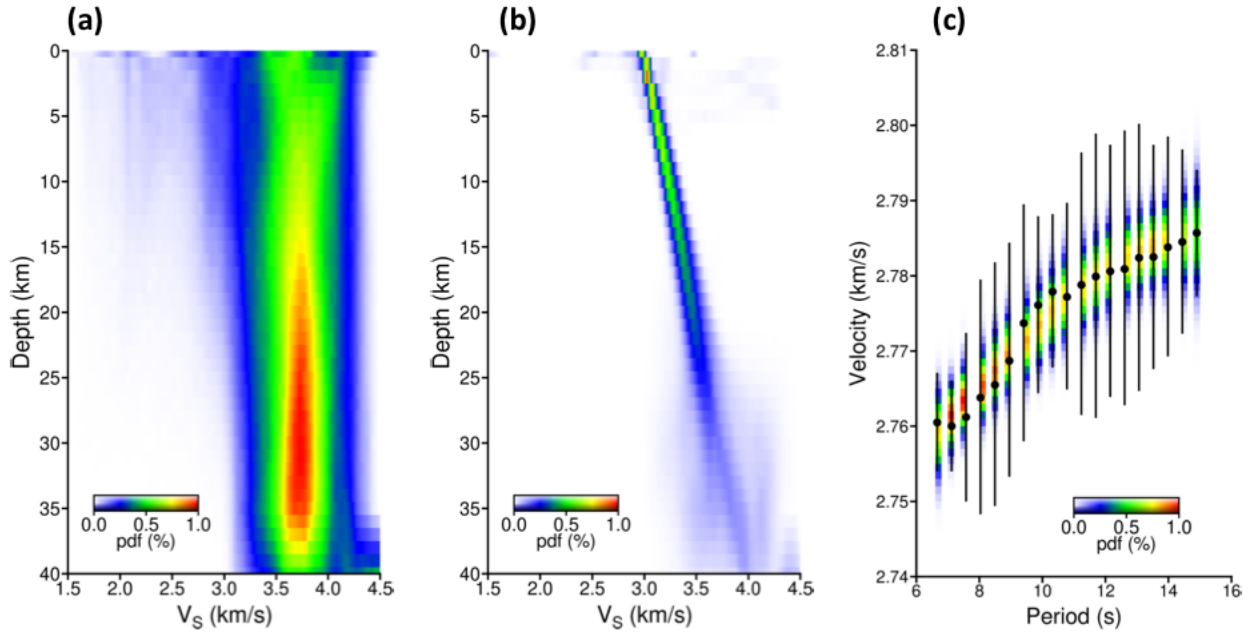

Figure S9. McMC Bézier inversion results. (a) a priori and (b) a posteriori Vs distributions. (c) a posteriori distribution of group velocities. Blue and red colors show small and large probabilities, respectively. Black dots correspond to the input data, and the 1 s uncertainties are shown with black vertical bars.

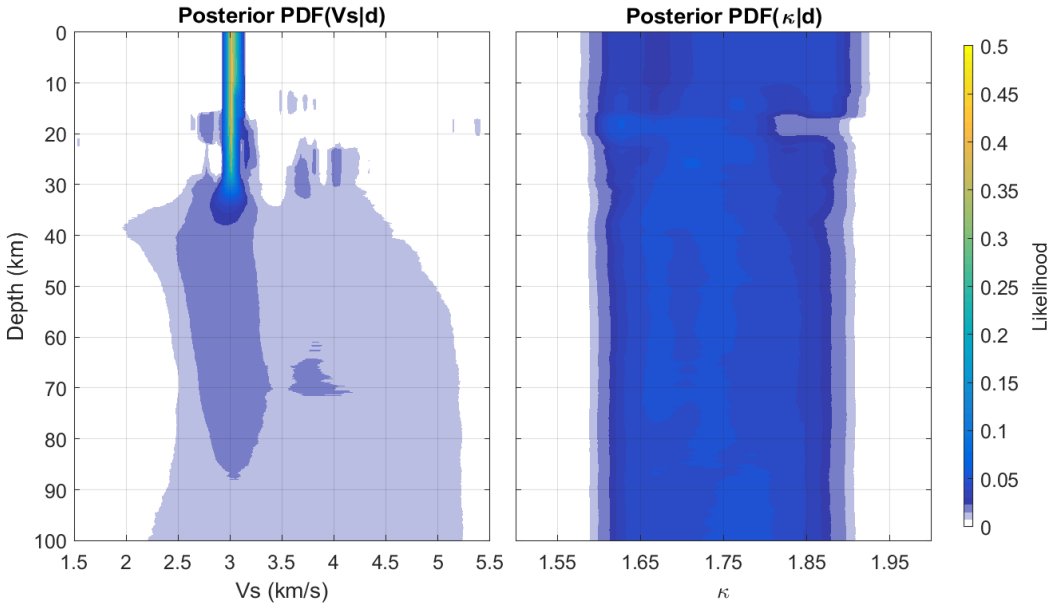

Figure S10. Vs (left) and κ (Vp/Vs ratio) (right) depth distributions retrieved using transdimensional Bayesian inversion of group velocity measurements of R1 in S1094b in the 8-15 s period range. The ensemble solutions are displayed as probability density functions at each depth, with warmer colors corresponding to higher posterior probabilities. Note the lack of κ resolution at all depths, and the lack of Vs resolution below ~30 km.

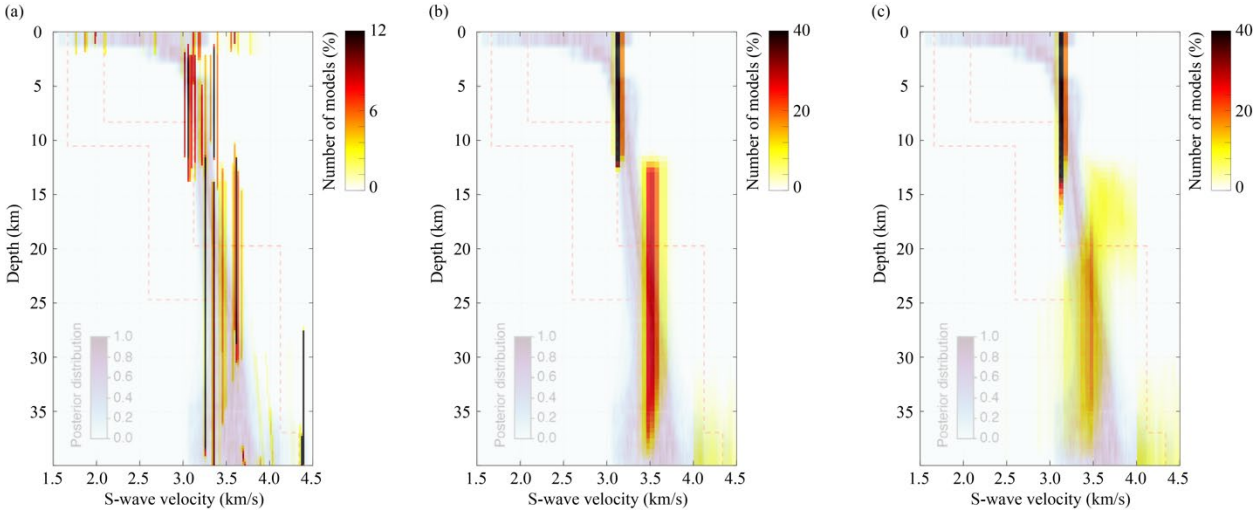

Figure S11. (a) Acceptable 80,000 models from the Niche Genetic Algorithm Inversion. The color scale corresponds to the model fraction. (b) and (c) Posterior distribution from TB rj-McMC Approach 3, separating the solutions with two (b) and three (c) crustal layers. In all figures, the transparent background is the posterior distribution from the McMC inversion in Fig. 2D.

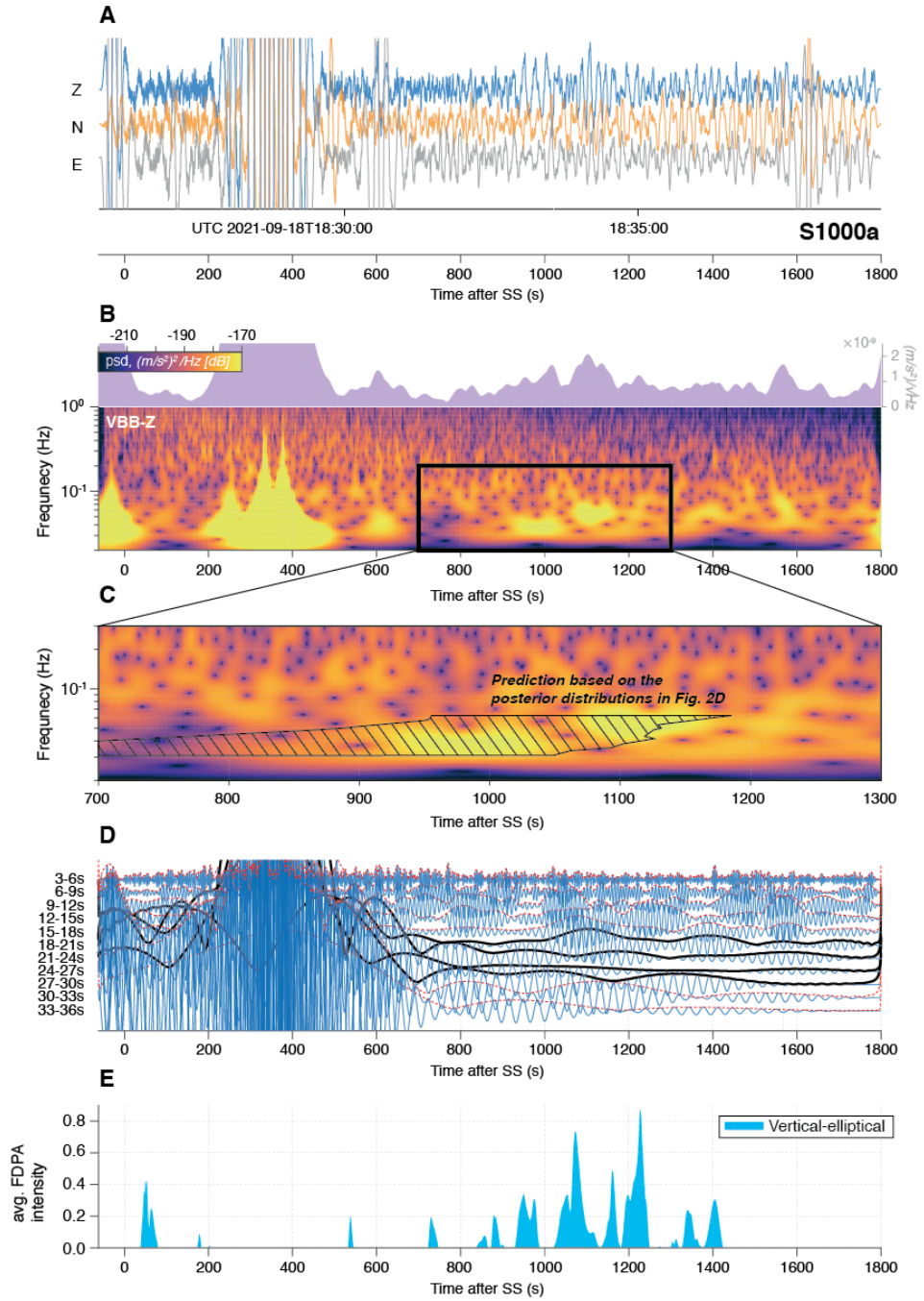

Figure S12. Summary of data processing of R1 arrival in S1000a. Details as Fig. S1-2 but for the signal associated with S1000a. (**A**) Raw three-component seismograms of event S1000a. (**B**) Vertical component S-transform spectrogram. The corresponding vertical envelope averaging the power spectral density across the 17-30 s period range is displayed at the top of the vertical spectrogram. (C) Zoom-in on S12B between 700 and 1300 s after the MQS SS pick. Two distinct long-period arrivals at ~20 s and ~ 30 s periods and the R1 group arrival time range predicted based on the posterior shown in Fig. 2D (hashed zone). (**D**) Narrow-band filter banks and envelopes. Black and red envelopes indicate the signals associated with the surface waves and noise, respectively. (**E**) Combined polarization metric averaged across 17-30 s (VEM) based on the FDPA.

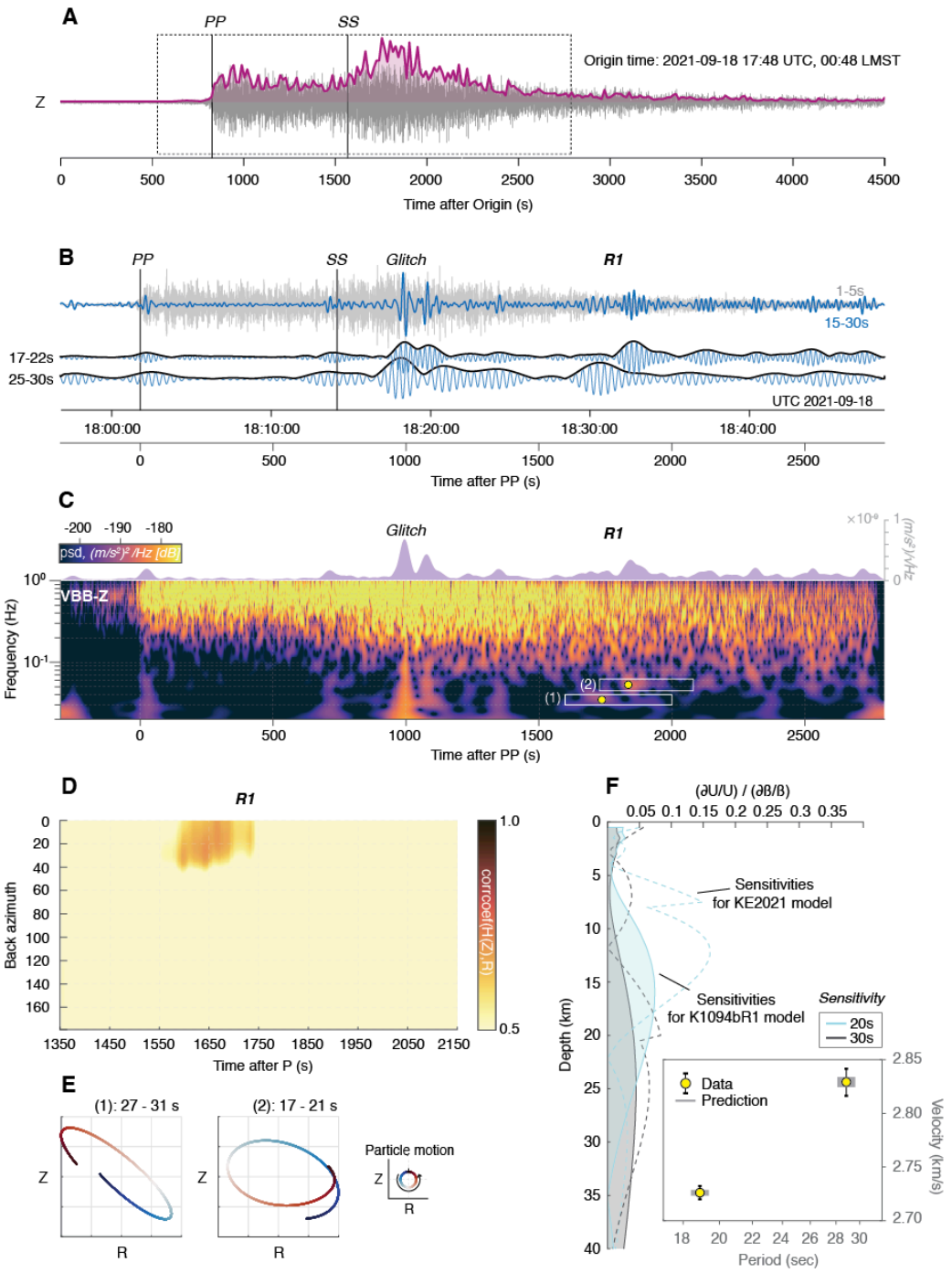

Figure S13. Observation of R1 in S1000a. (**A**) Vertical component times series of event S1000a bandpass filtered between 1-10 s and derived spectral envelope. (**B**) Zoom in of vertical-component seismogram bandpass filtered between 1-5 s (gray) and 15-30 s (blue) with PP and SS wave picks (black vertical lines). Narrow-band filter banks and envelopes show two distinct signals after 1500 s the PP-wave. (**C**) The vertical component S-transform of S1000a. (**D**) Back azimuth search of R1 arrivals in S1000a. The back azimuth estimates suggest that the first arriving ~ 30 s energy is compatible with the location of the crater associated with S1000a (*20*). No optimal back azimuth is determined for the ~ 20 s energy due to the environmental injection during the R1 window. Yellow dots in the spectrogram denotes the R1 measurements in S13F. (**E**) Hodograms constructed using vertical and radial component waveforms after rotating the raw horizontal

components with 32° back azimuth (based on the impact location). Retrograde particle motion of the R1 arrival is visible for both long-period energy at ~20 s and ~ 30 s periods. (**F**) Depth sensitivity kernels and data misfit of R1 in S1000a (inset). Two average group velocities are measured between 17-21 s and 27-31 s periods (yellow symbols). Kernels in dashed lines are computed based on the crustal model in (*7*). Shaded kernels and predictions are computed using the average model in Fig. 2E.

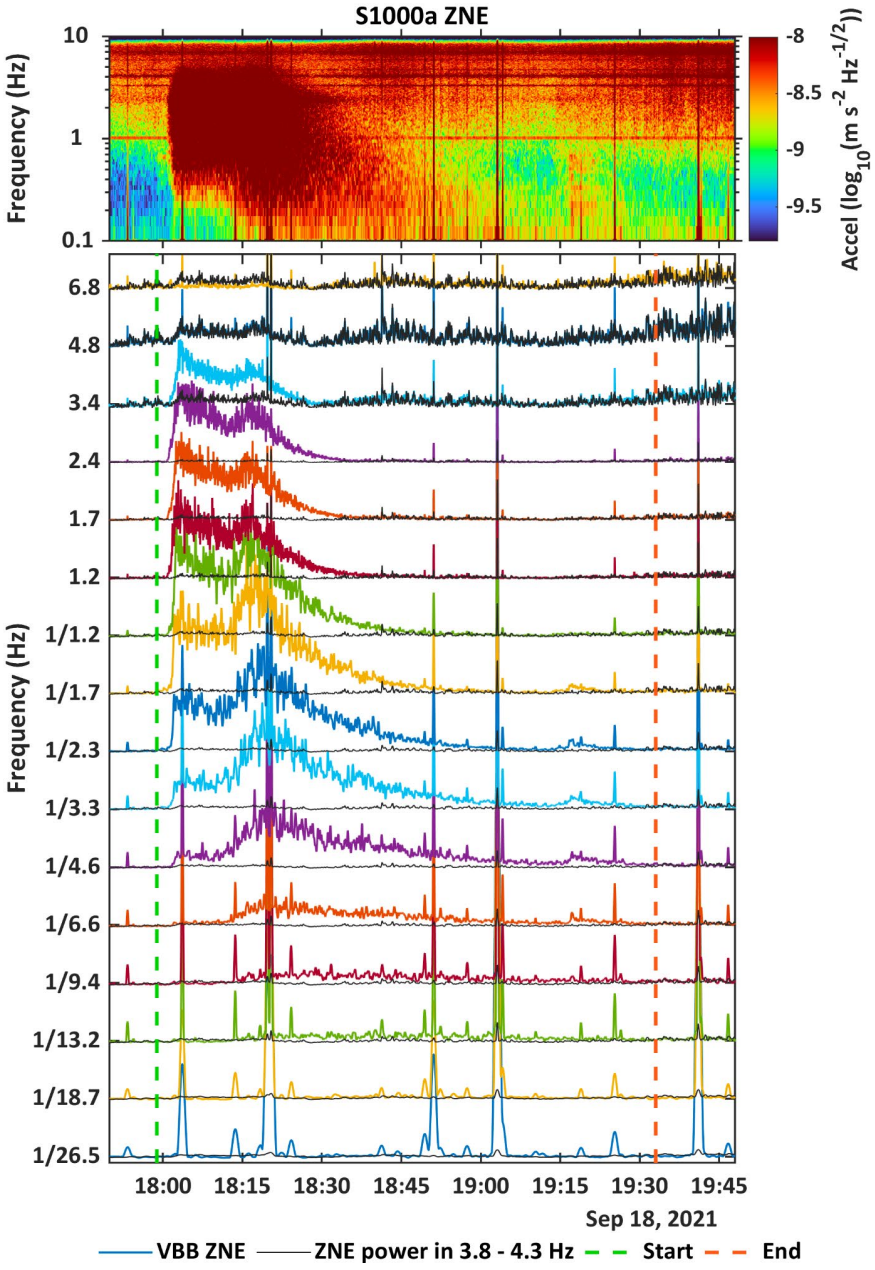

Figure S14. Comodulation analysis of S1000a. Details same as Fig. S3 and S5. The observed two distinct long-period energy (e.g., R1) discussed in S1000a section arrives within 18:27:00 - 18:35:00 UTC on Sept 18, 2021.

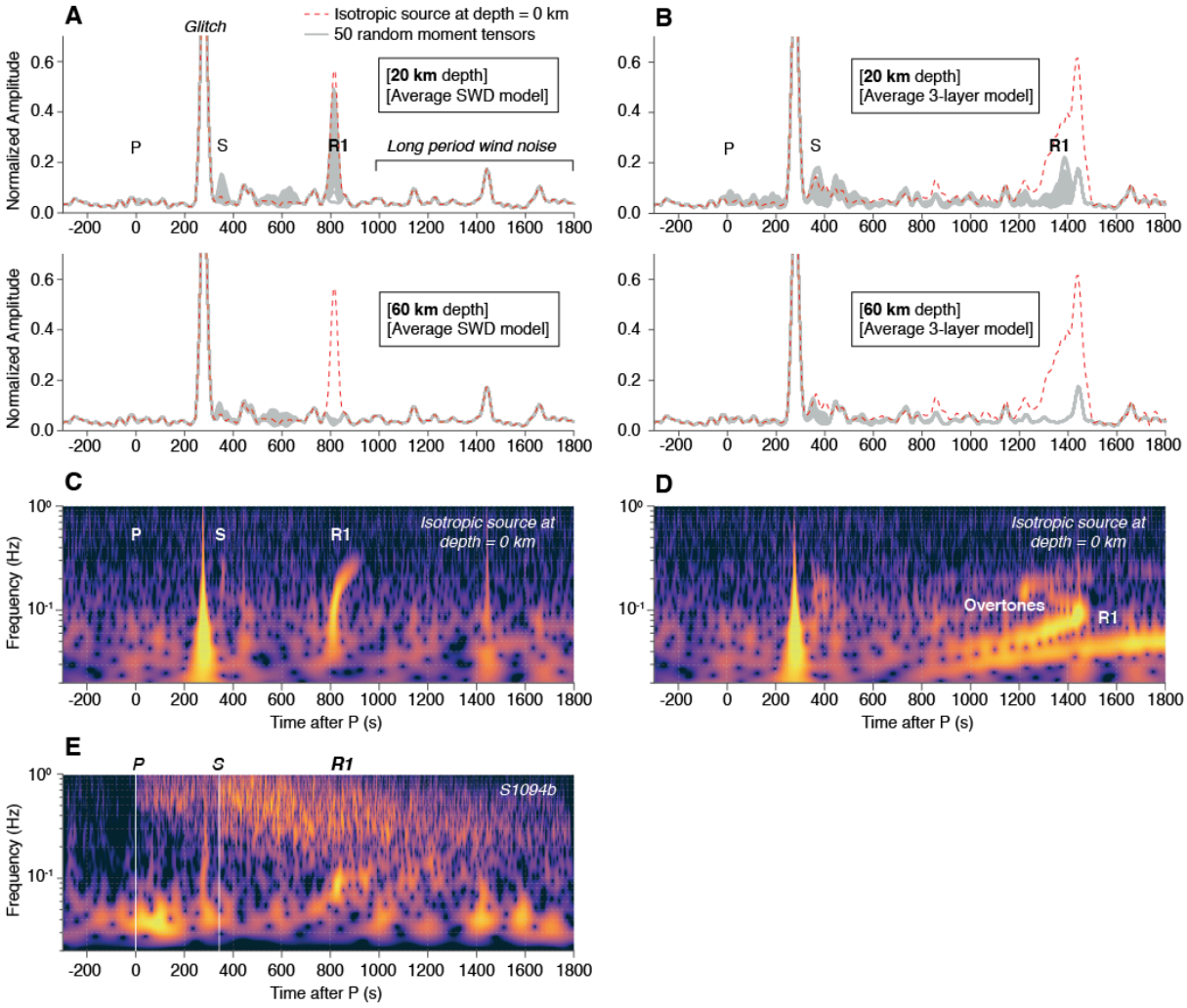

Figure S15. Summary of synthetic waveform simulation. (**A**) Vertical component envelopes computed based on the average crustal model in Fig. 2C with 50 random focal mechanisms. Source depths of 20 (top) and 60 km (bottom) are considered in the analysis. Envelopes are computed in the frequency domain by averaging power spectral density between 8-15 s period range. The corresponding envelope resulting from an isotropic source at the surface is shown in red. (**B**) Same as S14A but using a three-layer crustal model beneath the lander (*7*) with the mantle structure consistent to (*11*). (**C-D**) Comparison of the S-transform spectrograms derived from the two models used in S15A and S15B for an isotropic source at the surface. (**E**) Data S-transform spectrogram of S1094b shown in Fig. 2B.

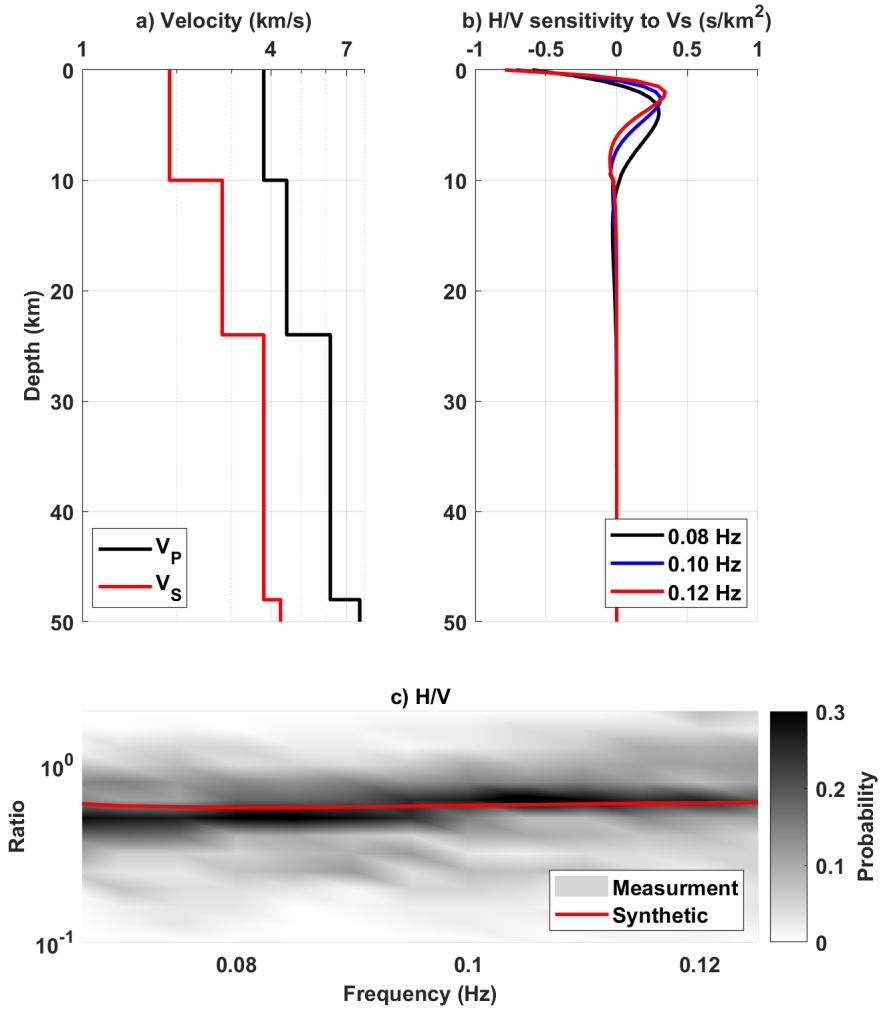

Figure S16. Summary of the H/V analysis. (**A**) Three-layer crustal velocity model used in the analysis (*7*) and (**B**) the corresponding H/V ratio depth sensitivity to S-wave velocity. (**C**) Comparison of the H/V ratio measurements for R1 arrival in S1094b and the synthetic prediction modeled using the model shown in S15A (red line). The gray color indicates the probability of the measured H/V ratios at each frequency.

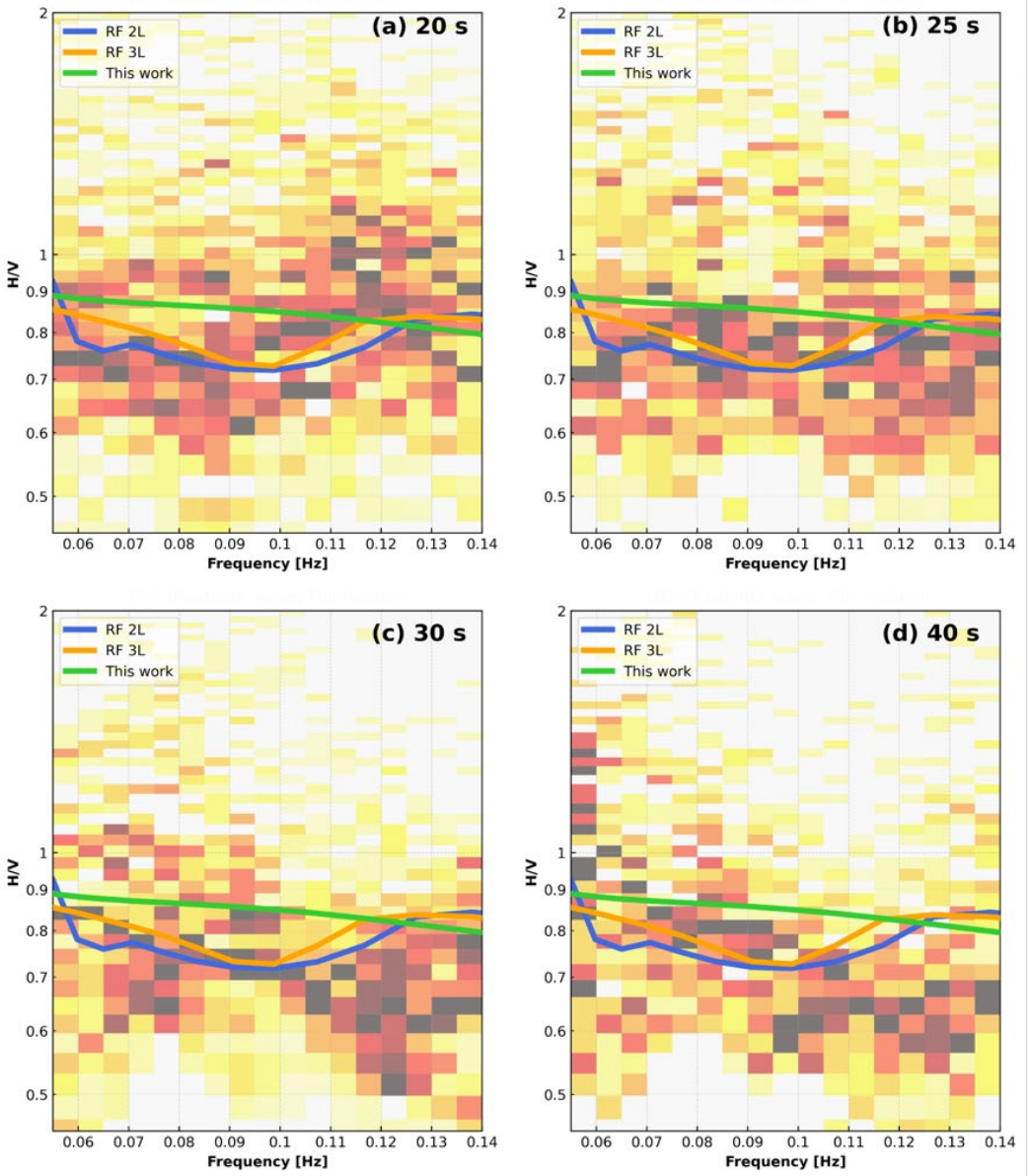

Figure S17. H/V measurements of the Rayleigh wave detected on December 24th, 2021 between 22:58:29.07 and 22:59:19.07 UTC. The different data density plots correspond to different time windows durations: (a) 20 s, (b) 25 s, (c) 30 s and (d) 40 s, using an overlapping factor of 98%. Darker colors indicate higher concentration of data. Predictions are made based on the representative of the martian crustal structure proposed by (*7*), with two (blue) and three (orange) layers, and this work (green).

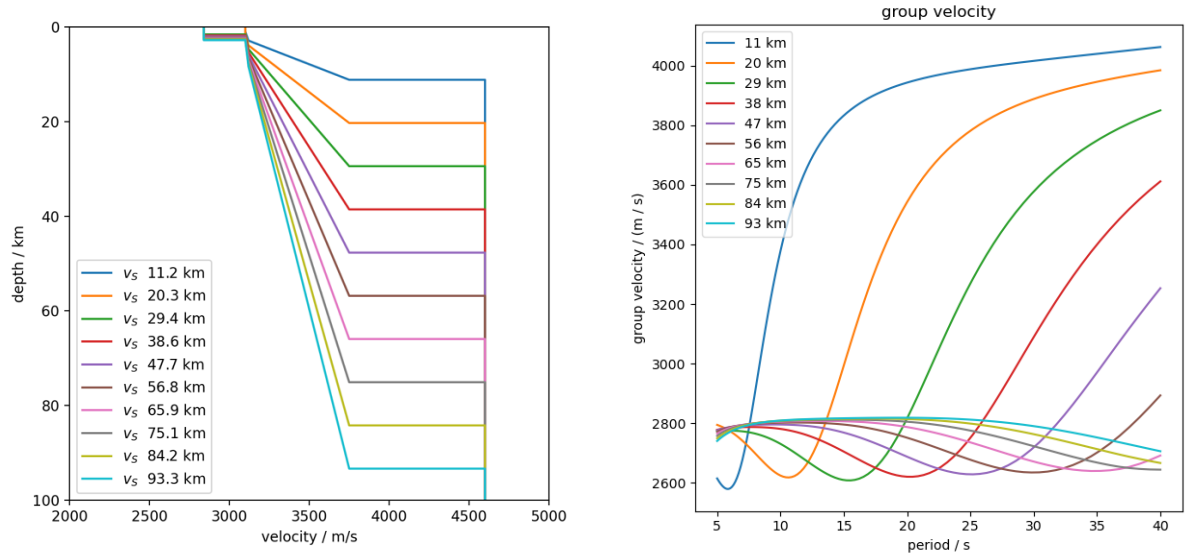

Figure S18. Velocity profiles (left) and corresponding group velocity curves (right) that go into calculating the global group velocity map scenario. The original model is the purple one labeled 47 km. For the modified crustal thicknesses, the Moho is moved and the linear gradient above the Moho is scaled linearly. In Hellas Planitia, the thickness is predicted to be below 15 km and thus, the bedrock layer is removed. All models produce an Airy phase with constant group velocity between 7 and 20 s period and a lower group velocity at longer periods, followed by a rapid increase in group velocity. This velocity minimum and the adjacent positive slope are moved to shorter periods for thinner crust. Thus slightly thinned crusts produce a delay, while crusts below 15 km thickness produce a strong advance in arrival time.

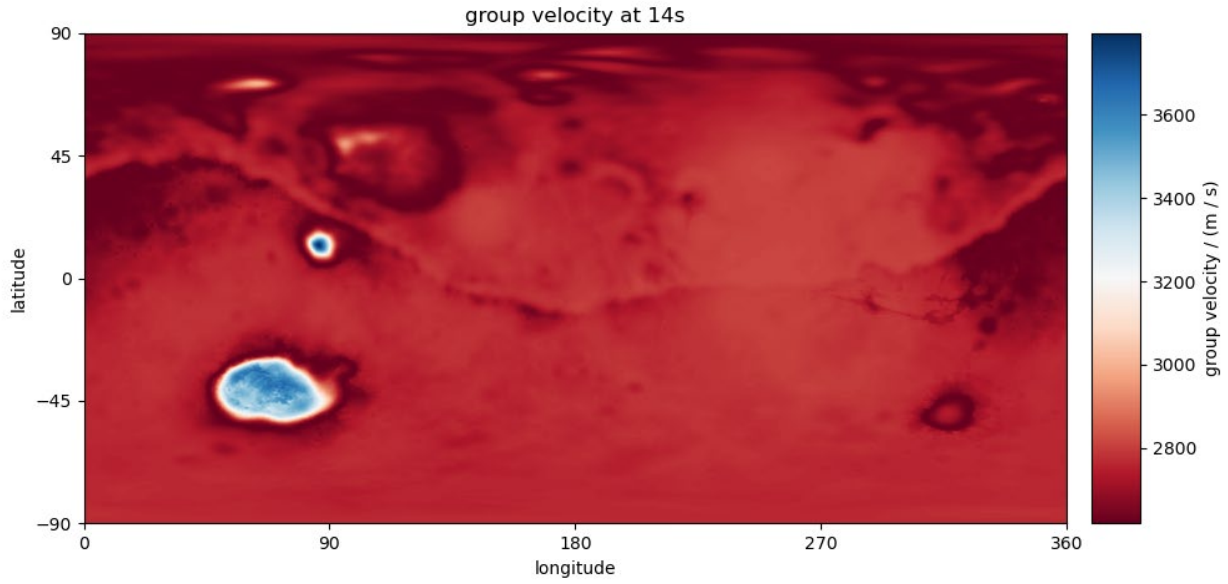

Figure S19. Proposed global group velocity map based on an average crustal density of 2550 kg/m^3 in the North and 2850 kg/m^3 in the South. At a period of 14 s, the global average is 2700-2900 m/s. Hellas Planitia is the single significant outlier on the R2 path of S1094b with group

velocity above 3400 m/s. The higher group velocities in Hellas Planitia can explain the higher overall group velocity of the R2 path.

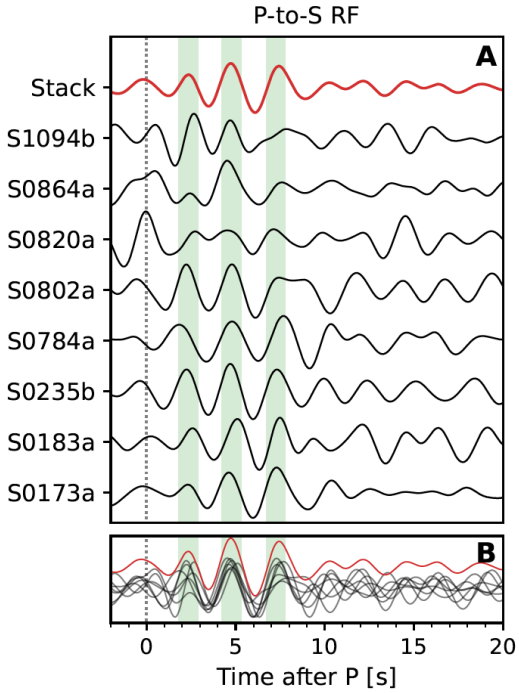

Figure S20. Summary of the RF analysis using eight LF family of events recorded by SEIS. (**A**) Observed P-to-s RFs for the events indicated on the left hand side of each trace. RFs are filtered between 2 s and 5 s. RF stack is shown in red. (B) All of the RFs shown in S20A are overlapped to enhance the visibility of the three coherent positive pulses (green bars) interpreted as the three crustal interfaces beneath the lander (*7*-*9*).

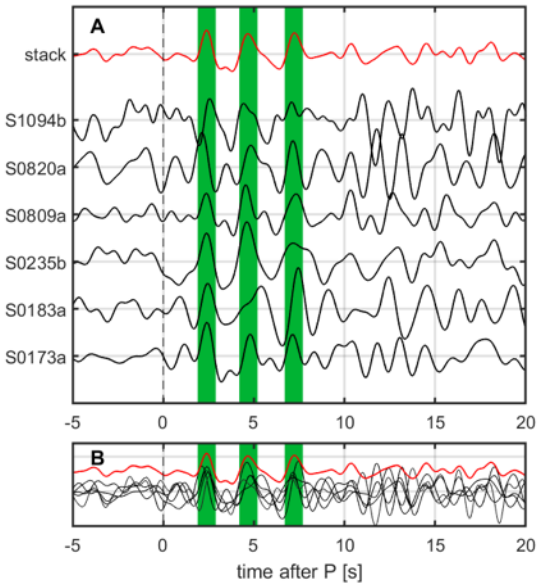

Figure S21. Summary of the RF analysis using LF families of events analyzed in (*7*) and (*9*). (**A**) Observed P-to-s RFs for the events indicated on the left hand side of each trace. These RFs are computed based on Method D described in (*7*). (**B**) All of the RFs shown in S21A are overlapped

to enhance the visibility of the three coherent positive pulses (green bars) interpreted as the three crustal interfaces beneath the lander (*7-9*).

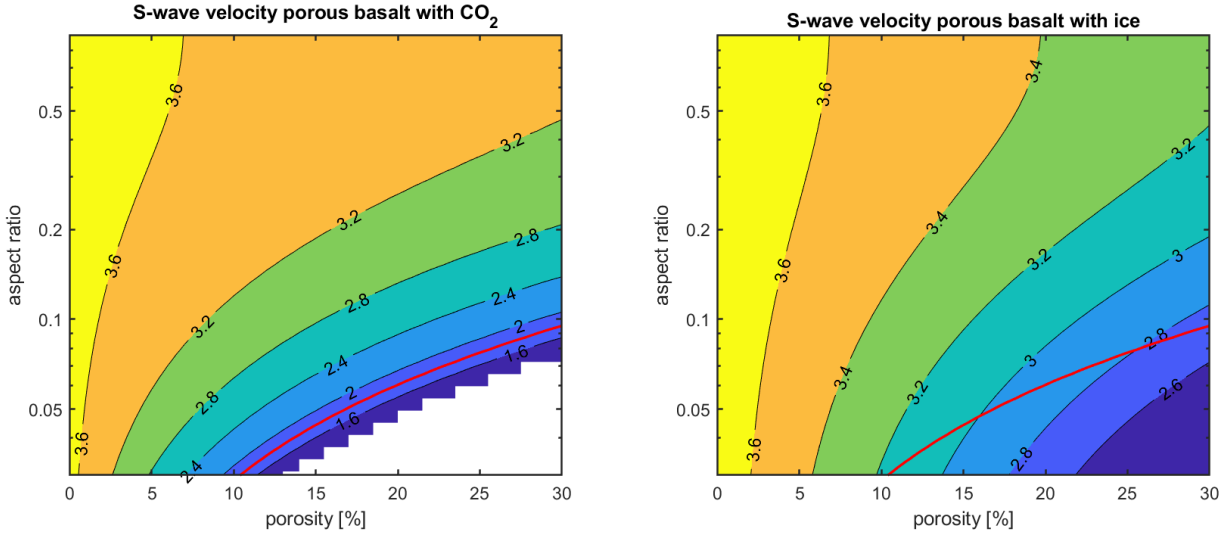

Figure S22. S-wave velocity in porous basalt derived from the self-consistent approximation for pores filled with CO_2 (left) and water ice (right), in relation to porosity and pore aspect ratio. Red trade-off curve on the left is for an S-wave velocity of 1.8 km/s, as observed in the uppermost approximately 10 km beneath the *InSight* lander (*7*), and is also drawn in the right sub-plot to indicate compatible velocities in case of ice-filled pores.